

1 ***Ab initio* Method for Examining the Halo Structure of ${}^6\text{He}$**

2 Mengyao Huang,^{1,*} Tobias Frederico,^{2,†} Pieter Maris,^{1,‡} Peng Yin,^{3,1,§}
3 Robert Basili,^{1,¶} Mark A. Caprio,^{4,**} Patrick J. Fasano,^{4,††} and James P. Vary^{1,‡‡}

4 *¹Department of Physics and Astronomy,*
5 *Iowa State University, Ames, Iowa, 50011, USA*

6 *²Instituto Tecnológico de Aeronáutica, DCTA,*
7 *12228-900 São José dos Campos, Brazil*

8 *³Institute of Modern Physics, Chinese Academy of Sciences, Lanzhou 730000, China*

9 *⁴Department of Physics and Astronomy,*
10 *University of Notre Dame, Notre Dame, Indiana 46556, USA*

11 (Dated: October 12, 2022)

Abstract

12

13 We solve for the ground states of ${}^4\text{He}$ and ${}^6\text{He}$ with *ab initio* configuration interaction methods
14 using the Daejeon16 nucleon-nucleon (NN) interaction. Using the full ground state wave functions,
15 we evaluate pairwise correlations to characterize the structures of these two systems. We use
16 coordinate-space pair correlations to address the halo structure of ${}^6\text{He}$ relative to ${}^4\text{He}$. We then
17 build a 3D analytic model followed by a 3D numerical model matching these correlation results.
18 Although these models are static and are classical candidate models for the preferred configuration
19 of the ground state of ${}^6\text{He}$, they provide an intuitive visualization of the ${}^6\text{He}$ nucleon spatial
20 correlations. We find a nearly planar configuration for the α cluster in ${}^6\text{He}$, and a nearly equilateral
21 triangle configuration for the center of mass of the α cluster with the two valence neutrons. Using a
22 modified 3D numerical model (M3DNM), we obtain the opening angle of the two valence neutrons
23 with respect to the center of mass of the α cluster $\theta_{nn} = 58.5^{+5.4}_{-6.2}$ degrees and root-mean-square
24 (rms) separation of the two valence neutrons $\sqrt{r_{nn}^2} = 4.12^{+0.37}_{-0.43}$ fm, both of which are consistent with
25 the results from a phenomenologically modified continuum-discretized coupled-channels (CDCC)
26 method. On the other hand, our θ_{nn} is $5^\circ \sim 15^\circ$ smaller than the unmodified CDCC result. The
27 upper bound of the estimated uncertainty of our $\sqrt{r_{nn}^2}$ is about 0.2 fm smaller than the lower
28 bound of uncertainty of the experimental value obtained by an interferometry technique.

29 I. INTRODUCTION

30 Clustering phenomena within the atomic nucleus have long been an attractive topic to
31 nuclear physicists, since it bridges the degrees of freedom of individual nucleons to possible
32 collective structures within the nucleus. As a natural example, certain nuclei near the “drip
33 lines” (where nucleons are free to escape) form a more tightly bound core and a “halo” made
34 of one or more nucleons loosely bound to the core [1–5].

* mengyaoh@iastate.edu

† tobias@ita.br

‡ pmaris@iastate.edu

§ yinpeng@impcas.ac.cn

¶ basiliro@iastate.edu

** mcaprio@nd.edu

†† pfasano@nd.edu

‡‡ jvary@iastate.edu

35 Neutron halos have drawn significant attention since the 1980s when the surprisingly large
36 interaction cross section of ^{11}Li compared with other Li isotopes was observed in radioactive
37 ion beams (RIB) transmission experiments [6–8]. They also display a narrow core momentum
38 distribution in peripheral breakup reactions [9, 10]. Strong electric dipole ($E1$) excitations
39 at low excitation energy were observed in some of the halo nuclei, attributed to their weakly
40 bound halo neutron(s) undergoing excitation to the continuum states [11–13]. Although
41 there is no clear-cut distinction between the halo and non-halo nuclei, halo nuclei possess
42 some common features. Nuclei with a neutron halo, for example, present a long tail in the
43 density distribution profile, and have exceptionally small neutron separation energies for the
44 halo neutron(s).

45 Over the years, many efforts have been made to extract the clustering information from
46 *ab initio* calculations. The *ab initio* NCSM/RGM (no-core shell model/resonating group
47 method) was used to perform calculations on a $^4\text{He}(\text{g.s.})+n+n$ cluster basis which was
48 consistent with *ab initio* NCSM calculations without a cluster basis [14–16]. Cluster form
49 factors were extracted [17], and further improvements have been made to the work of three-
50 cluster dynamics within *ab initio* no-core shell model with continuum [16, 18]. The *ab*
51 *initio* lattice approach implementing chiral effective field theory successfully modeled a $3-\alpha$
52 structure for the Hoyle state of ^{12}C [19]. More recently, *ab initio* configuration interaction
53 methods have revealed important roles of α -clustering in light nuclei including details on the
54 ground and Hoyle excited state of ^{12}C [20]. In addition, measures of entanglement of ^4He
55 and ^6He nuclei were explored using *ab initio* nuclear many-body calculations [21], where a
56 core-valence structure naturally emerges from the full no-core calculation of ^6He by analyzing
57 common features of entanglement.

58 From a computational point of view, studying the clustering properties of nuclei could
59 help us design improved basis functions and to usefully subdivide the Hilbert space into
60 regions of greater and lesser importance. Spatial information such as the average relative
61 separations of nucleons in a system is key to characterizing the cluster wave functions.

62 To this end, we propose a novel method for extracting the semi-classical spatial infor-
63 mation from *ab initio* calculations, utilizing two-body observables. Previously, one-body
64 observables have been used in the *ab initio* NCSM [22] with great success in revealing in-
65 formation on the clustering of Li isotopes [23, 24] and ^9Be [24], which is a one-neutron halo
66 nucleus. Using two-body operators has the advantage of unfolding the detailed structure

67 of the dominant configuration, reflecting the differences in the nucleon-nucleon correlations
68 among the pairs of nucleons.

69 We choose ${}^6\text{He}$ as a test case for this new method owing to its relative simplicity. It is
70 the lightest Borromean halo nucleus which means that none of the available two-component
71 substructure (n - n or n - α in the $\alpha+n+n$ system) is bound when one removes any third
72 component. In this case, one-body observables can smear out the structure for the $2n$ -
73 halo, while two-body observables can explore the relative distance between the two valence
74 neutrons compared with the relative distances of the other pairs of nucleons. Our primary
75 focus is to introduce our method and demonstrate its application to ${}^6\text{He}$ in advance of
76 achieving fully converged *ab initio* NCSM results for the two-body observables that we
77 develop and employ. We defer the development of suitable extrapolation methods for these
78 two-body observables to a later project.

79 In the following sections, we first introduce the two-body operators we will use (Sec. II)
80 and the approach to solving the quantum many-body problem (Sec. III). We then present
81 and discuss the calculated expectation values of these two-body operators (Sec. IV). Follow-
82 ing that, we introduce a 3D analytic model using our calculated two-body observables and
83 find that the halo structure of ${}^6\text{He}$ can be realized with some major features (Sec. V-A).
84 Later on, we construct a 3D numerical model, which removes the geometric assumptions in
85 the analytic model (Sec. V-B). Finally, this model is modified by introducing a parameter
86 that accounts for a difference between two pairs previously assumed to share the same value
87 of root-mean-square pair distance (Sec. V-C). We compare the geometrical information
88 characterized by the opening angle θ_{nn} and neutron-neutron (nn) rms separation $\sqrt{r_{nn}^2}$ of
89 the two valence neutrons extracted using our modified 3D numerical model with the values
90 obtained from an interferometry experiment and obtained from theory with the unmodi-
91 fied/modified CDCC method (Sec. V-C). We provide additional discussion and conclusions
92 in Sec. VI.

93 II. CONSTRUCTING TWO-BODY OPERATORS IN COUPLED- J BASIS

94 In order to carry out a quantitative analysis of the distributions of nucleons and pairs of
95 nucleons within a nucleus, we require appropriate operators that sample these quantities.
96 For this purpose, we will define useful one-body and two-body operators whose expectation

97 values within the nuclear ground state will inform our detailed analysis of how nucleons are
 98 arranged in coordinate space on average. From this arrangement, we hope to infer if a halo
 99 structure is emerging from the quantum many-body wave functions.

100 **A. One- and two-body operators in the occupation representation**

101 One-body operators are defined as

$$\mathcal{O}_{1B} = \sum_{\alpha,\beta} O_{\alpha\beta} a_{\alpha}^{\dagger} a_{\beta}, \quad (1)$$

102 where

$$O_{\alpha\beta} = \langle \alpha | \mathcal{O} | \beta \rangle \quad (2)$$

103 are the one-body matrix elements with the Greek subscripts label the single-particle states
 104 in an ordered sequence. The single-particle states are related to creation operators acting
 105 on the vacuum,

$$|\alpha\rangle = a_{\alpha}^{\dagger} |0\rangle. \quad (3)$$

106 Similarly, two-body operators are defined as

$$\mathcal{O}_{2B} = \sum_{\alpha<\beta,\gamma<\delta} O_{\alpha\beta\gamma\delta} a_{\alpha}^{\dagger} a_{\beta}^{\dagger} a_{\delta} a_{\gamma}, \quad (4)$$

107 where

$$O_{\alpha\beta\gamma\delta} = \langle \alpha\beta | \mathcal{O} | \gamma\delta \rangle = \langle 0 | a_{\beta} a_{\alpha} \mathcal{O} a_{\gamma}^{\dagger} a_{\delta}^{\dagger} | 0 \rangle \quad (5)$$

108 are the two-body matrix elements. Due to the fermion anticommutation relation $a_{\alpha}^{\dagger} a_{\beta}^{\dagger} =$
 109 $-a_{\beta}^{\dagger} a_{\alpha}^{\dagger}$ for $\alpha \neq \beta$, the two-body matrix elements are antisymmetric for each pair of two-body
 110 state labels.

111 From now on, we will focus only on the two-body operators. The expectation value of
 112 a two-body operator between an initial state $|\Phi_A\rangle$ and a final state $|\Phi'_A\rangle$ in a system of
 113 nucleons is thus

$$\langle \Phi'_A | \mathcal{O}_{2B} | \Phi_A \rangle = \sum_{\alpha\beta\gamma\delta} \rho_{\alpha\beta\gamma\delta} \langle \alpha\beta | \mathcal{O} | \gamma\delta \rangle, \quad (6)$$

114 where $\alpha < \beta, \gamma < \delta$ is implicitly assumed wherever summing pairs of two-body state labels,
 115 and

$$\rho_{\alpha\beta\gamma\delta} = \langle \Phi'_A | a_{\alpha}^{\dagger} a_{\beta}^{\dagger} a_{\delta} a_{\gamma} | \Phi_A \rangle \quad (7)$$

116 is called the two-body density matrix.

117 **B. Two-body operators in the coupled- J basis**

118 The standard basis we use is the single particle basis, which is denoted by its quantum
 119 numbers including radial quantum number n , orbital angular momentum (AM) l , spin s ,
 120 total AM j , total AM projection m_j , isospin τ and isospin projection τ_z . We can use the
 121 short-hand notation

$$\alpha = \{n_\alpha, l_\alpha, \frac{1}{2}, j_\alpha, m_{j_\alpha}, \frac{1}{2}, \tau_{z\alpha}\}, \quad (8)$$

122 where the first “1/2” is for nucleon spin s and the second “1/2” is for nucleon isospin τ .

123 In order to compute matrix elements of two-body operators in a basis with “good” AM
 124 which is the two-body total AM J , we perform a transformation using Clebsch-Gordan
 125 coefficients:

$$\{a_\alpha^\dagger a_\beta^\dagger\}_{J,M} = \sum_{m_{j_\alpha}, m_{j_\beta}} C_{m_{j_\alpha} m_{j_\beta} M}^{j_\alpha j_\beta J} a_\alpha^\dagger a_\beta^\dagger, \quad (9)$$

126 where M is the z -projection of J . The transformed basis is called coupled- J basis or J basis
 127 for short. Sometimes, it is also referred to as the “ jj -coupled basis”.

128 The two-body density matrix in the J basis, suppressing the z -projection quantum num-
 129 ber M for compactness of notation, is

$$\begin{aligned} \rho_{\{\alpha\beta\}_{J'}\{\gamma\delta\}_J} &= \langle \Phi'_A | \{a_\alpha^\dagger a_\beta^\dagger\}_{J'} \{a_\delta a_\gamma\}_J | \Phi_A \rangle \\ &= \sum_{m_{j_\alpha}, m_{j_\beta}} C_{m_{j_\alpha} m_{j_\beta} M'}^{j_\alpha j_\beta J'} \sum_{m_{j_\gamma}, m_{j_\delta}} C_{m_{j_\gamma} m_{j_\delta} M}^{j_\gamma j_\delta J} \rho_{\alpha\beta\gamma\delta}. \end{aligned} \quad (10)$$

130 The expectation value of a two-body operator in a system of nucleons expressed in the J
 131 basis can thus be written as

$$\langle \Phi_{A'} | \mathcal{O}_{2B} | \Phi_A \rangle = \sum_{\{\alpha\beta\}_{J'}\{\gamma\delta\}_J} \rho_{\{\alpha\beta\}_{J'}\{\gamma\delta\}_J} \langle \alpha\beta; J' | \mathcal{O} | \gamma\delta; J \rangle, \quad (11)$$

132 where \mathcal{O} is redefined as an operator acting on J basis and

$$|\alpha\beta; J\rangle = \{a_\alpha^\dagger a_\beta^\dagger\}_J |0\rangle. \quad (12)$$

133 When one aims to calculate observables solely represented by one-body and two-body
 134 operators, it is often advantageous for efficient use of storage to compute and store the one-
 135 body and two-body density matrices between the desired initial and final states rather than
 136 the full nuclear wave functions.

137 **C. Rotationally invariant scalar operator with given two-body total spin and given**
 138 **pair of isospin projections**

139 We define a rotationally invariant scalar operator with given two-body total spin as

$$\mathcal{O}(r)[S] \equiv O(r)P_S, \quad (13)$$

140 where $O(r)$ is a scalar operator with spherical symmetry, and P_S is a two-body total spin
 141 projection operator. Since the $O(r)$ operator is a rank-0 tensor, from the Wigner-Eckart
 142 theorem,

$$\langle \alpha\beta; J' | \mathcal{O}(r) | \gamma\delta; J \rangle = \delta_{J'J} \delta_{M'M} \langle \alpha\beta; J || O(r) || \gamma\delta; J \rangle. \quad (14)$$

143 where, in our convention, the double-bar (reduced) matrix element does not factor out
 144 $(2J+1)^{-\frac{1}{2}}$ and remains consistent with the Wigner-Eckart theorem formulated in Eq. (4.20)
 145 of Ref. [25].

146 In order to select the states of given two-body total spin, one can resolve quantities in
 147 terms of two-body total spin S ($\vec{S} = \vec{s}_\alpha + \vec{s}_\beta$) and two-body total orbital AM λ ($\vec{\lambda} = \vec{l}_\alpha + \vec{l}_\beta$)
 148 by inserting

$$\mathbb{1} = \sum_{\lambda S} |n_\alpha l_\alpha n_\beta l_\beta \lambda, \frac{1}{2} \frac{1}{2} S; J\rangle \langle n_\alpha l_\alpha n_\beta l_\beta \lambda, \frac{1}{2} \frac{1}{2} S; J| \quad (15)$$

149 twice, where the spin quantum numbers ($\frac{1}{2}$) are explicit while the isospin quantum numbers
 150 are omitted for simplification of the notation. z -projections are suppressed in all the following
 151 derivations until the end of Section II C.

152 With $\langle S_1 | P_S | S_2 \rangle = \delta_{S S_1} \delta_{S_1 S_2}$ and Eq. (13), (14), we have

$$\begin{aligned} & \langle \alpha\beta; J' | \mathcal{O}(r)[S] | \gamma\delta; J \rangle = \delta_{J'J} \delta_{M'M} \langle \alpha\beta; J || O(r) P_S || \gamma\delta; J \rangle \\ &= \delta_{J'J} \delta_{M'M} \sum_{\lambda_1 S_1} \sum_{\lambda_2 S_2} \langle \alpha\beta; J | n_\alpha l_\alpha n_\beta l_\beta \lambda_1, \frac{1}{2} \frac{1}{2} S_1; J \rangle \\ & \quad \times \langle n_\alpha l_\alpha n_\beta l_\beta \lambda_1, \frac{1}{2} \frac{1}{2} S_1; J || O(r) \delta_{S S_1} \delta_{S_1 S_2} || n_\gamma l_\gamma n_\delta l_\delta \lambda_2, \frac{1}{2} \frac{1}{2} S_2; J \rangle \langle n_\gamma l_\gamma n_\delta l_\delta \lambda_2, \frac{1}{2} \frac{1}{2} S_2; J | \gamma\delta; J \rangle \\ &= \delta_{J'J} \delta_{M'M} \sum_{\lambda_1} \sum_{\lambda_2} \langle \alpha\beta; J | n_\alpha l_\alpha n_\beta l_\beta \lambda_1, \frac{1}{2} \frac{1}{2} S; J \rangle \langle n_\alpha l_\alpha n_\beta l_\beta \lambda_1; J || O(r) || n_\gamma l_\gamma n_\delta l_\delta \lambda_2; J \rangle \\ & \quad \times \langle n_\gamma l_\gamma n_\delta l_\delta \lambda_2, \frac{1}{2} \frac{1}{2} S; J | \gamma\delta; J \rangle \\ &= \delta_{J'J} \delta_{M'M} \sum_{\lambda} \langle \alpha\beta; J | n_\alpha l_\alpha n_\beta l_\beta \lambda, \frac{1}{2} \frac{1}{2} S; J \rangle \langle n_\alpha l_\alpha n_\beta l_\beta \lambda || O(r) || n_\gamma l_\gamma n_\delta l_\delta \lambda \rangle \langle n_\gamma l_\gamma n_\delta l_\delta \lambda, \frac{1}{2} \frac{1}{2} S; J | \gamma\delta; J \rangle, \end{aligned} \quad (16)$$

153 where in the last line we have used the fact that $O(r)$ is rotationally invariant so the two-body
 154 total orbital AM is invariant upon the action of $O(r)$, i.e. $\langle \lambda_1 | O(r) | \lambda_2 \rangle = \langle \lambda_1 | O(r) \delta_{\lambda_1 \lambda_2} | \lambda_2 \rangle$.
 155 And we drop the subscript of λ at the end for simplification of the notation. There is no need
 156 to label J values in the reduced matrix elements, because $O(r)$ only produces a dependence
 157 on the radial and orbital quantum numbers.

158 We identify the $LS - jj$ coupling coefficient [26] in (16) by first expanding the notation

$$\begin{aligned}
 \langle \alpha\beta; J | n_\alpha l_\alpha n_\beta l_\beta \lambda, \frac{1}{2} \frac{1}{2} S; J \rangle &= \langle n_\alpha l_\alpha \frac{1}{2} j_\alpha, n_\beta l_\beta \frac{1}{2} j_\beta; J | n_\alpha l_\alpha n_\beta l_\beta \lambda, \frac{1}{2} \frac{1}{2} S; J \rangle \\
 &= \langle l_\alpha \frac{1}{2} j_\alpha, l_\beta \frac{1}{2} j_\beta; J | l_\alpha l_\beta \lambda, \frac{1}{2} \frac{1}{2} S; J \rangle \\
 &= \sqrt{(2j_\alpha + 1)(2j_\beta + 1)(2\lambda + 1)(2S + 1)} \left\{ \begin{array}{ccc} l_\alpha & l_\beta & \lambda \\ 1/2 & 1/2 & S \\ j_\alpha & j_\beta & J \end{array} \right\}, \quad (17)
 \end{aligned}$$

159 where the curly brackets represent the $9j$ symbols, which is another way to write an assembly
 160 of Clebsch-Gordan coefficients.

161 One then obtains

$$\begin{aligned}
 \langle \alpha\beta; J' | \mathcal{O}(r) [S] | \gamma\delta; J \rangle &= \delta_{J'J} \delta_{M'M} \\
 &\times (2S + 1) \sqrt{(2j_\alpha + 1)(2j_\beta + 1)(2j_\gamma + 1)(2j_\delta + 1)} \sum_\lambda (2\lambda + 1) \left\{ \begin{array}{ccc} l_\alpha & l_\beta & \lambda \\ 1/2 & 1/2 & S \\ j_\alpha & j_\beta & J \end{array} \right\} \left\{ \begin{array}{ccc} l_\gamma & l_\delta & \lambda \\ 1/2 & 1/2 & S \\ j_\gamma & j_\delta & J \end{array} \right\} \\
 &\times \langle n_\alpha l_\alpha n_\beta l_\beta \lambda | \mathcal{O}(r) | n_\gamma l_\gamma n_\delta l_\delta \lambda \rangle. \quad (18)
 \end{aligned}$$

162 To apply this operator on a fixed pair of isospin z -projection values for two nucleons
 163 within a system of nucleons, we can construct an operator, preserving normalization when
 164 $\tau_{za} = \tau_{zb}$ by including the factor $(1 - \delta_{\tau_{za}, \tau_{zb}})$,

$$\mathcal{B}(r) [S, \tau_{za}, \tau_{zb}] \equiv \sum_{i < j} \mathcal{O}(r_{ij}) [S, \tau_{za}, \tau_{zb}] = \sum_{i < j} \mathcal{O}(r_{ij}) [S] (\delta_{\tau_{zi}, \tau_{za}} \delta_{\tau_{zj}, \tau_{zb}} + (1 - \delta_{\tau_{za}, \tau_{zb}}) \delta_{\tau_{zi}, \tau_{zb}} \delta_{\tau_{zj}, \tau_{za}}), \quad (19)$$

165 where i, j run through all nucleons in the system with $i < j$ and $r_{ij} = |\vec{r}_i - \vec{r}_j|$. It follows

166 that

$$\begin{aligned}
& \langle \alpha\beta; J' | \mathcal{B}(r) [S, \tau_{za}, \tau_{zb}] | \gamma\delta; J \rangle \\
&= \langle \alpha\beta; J' | \mathcal{B}(r) [S, \tau_{za}, \tau_{zb}] \delta_{\tau_{z\alpha}, \tau_{z\gamma}} \delta_{\tau_{z\beta}, \tau_{z\delta}} | \gamma\delta; J \rangle \\
&= \langle \alpha\beta; J' | \mathcal{O}(r_{\alpha\beta}) [S, \tau_{za}, \tau_{zb}] \delta_{\tau_{z\alpha}, \tau_{z\gamma}} \delta_{\tau_{z\beta}, \tau_{z\delta}} | \gamma\delta; J \rangle \\
&= \langle \alpha\beta; J' | \mathcal{O}(r) [S] | \gamma\delta; J \rangle \left(\delta_{\tau_{z\alpha}, \tau_{za}} \delta_{\tau_{z\beta}, \tau_{zb}} + (1 - \delta_{\tau_{za}, \tau_{zb}}) \delta_{\tau_{z\alpha}, \tau_{zb}} \delta_{\tau_{z\beta}, \tau_{za}} \right) \delta_{\tau_{z\alpha}, \tau_{z\gamma}} \delta_{\tau_{z\beta}, \tau_{z\delta}},
\end{aligned} \tag{20}$$

167 where in the second line we have included the definition that the isospin z -projections are
168 fixed.

169 The resulting matrix elements become

$$\begin{aligned}
& \langle \alpha\beta; J' M' | \mathcal{B}(r) [S, \tau_{za}, \tau_{zb}] | \gamma\delta; J M \rangle = \left(\delta_{\tau_{z\alpha}, \tau_{za}} \delta_{\tau_{z\beta}, \tau_{zb}} + (1 - \delta_{\tau_{za}, \tau_{zb}}) \delta_{\tau_{z\alpha}, \tau_{zb}} \delta_{\tau_{z\beta}, \tau_{za}} \right) \delta_{\tau_{z\alpha}, \tau_{z\gamma}} \delta_{\tau_{z\beta}, \tau_{z\delta}} \\
& \times \delta_{J' J} \delta_{M' M} (2S + 1) \sqrt{(2j_\alpha + 1)(2j_\beta + 1)(2j_\gamma + 1)(2j_\delta + 1)} \\
& \times \sum_\lambda (2\lambda + 1) \begin{Bmatrix} l_\alpha & l_\beta & \lambda \\ 1/2 & 1/2 & S \\ j_\alpha & j_\beta & J \end{Bmatrix} \begin{Bmatrix} l_\gamma & l_\delta & \lambda \\ 1/2 & 1/2 & S \\ j_\gamma & j_\delta & J \end{Bmatrix} \langle n_\alpha l_\alpha n_\beta l_\beta \lambda \mu | | \mathcal{O}(r) | | n_\gamma l_\gamma n_\delta l_\delta \lambda \mu \rangle.
\end{aligned} \tag{21}$$

170 D. Pair-identity operator

171 The pair-identity operator for a fixed pair of isospin projections and a fixed two-body
172 total spin S works as a projection operator on a subspace of two-body total S and isospin
173 projection pair sector,

$$r^0[S, \tau_{za}, \tau_{zb}] \equiv \sum_{i < j} P_S \left(\delta_{\tau_{zi}, \tau_{za}} \delta_{\tau_{zj}, \tau_{zb}} + (1 - \delta_{\tau_{za}, \tau_{zb}}) \delta_{\tau_{zi}, \tau_{zb}} \delta_{\tau_{zj}, \tau_{za}} \right). \tag{22}$$

174 Compared with (19) and (20), this is the same as setting

$$O(r) = r^0. \tag{23}$$

175 Summing over S in (22) gives

$$r^0[\tau_{za}, \tau_{zb}] \equiv \sum_{i < j} \left(\delta_{\tau_{zi}, \tau_{za}} \delta_{\tau_{zj}, \tau_{zb}} + (1 - \delta_{\tau_{za}, \tau_{zb}}) \delta_{\tau_{zi}, \tau_{zb}} \delta_{\tau_{zj}, \tau_{za}} \right), \tag{24}$$

176 whose expectation value is an integer that equals to the number of pairs in a fixed pair of
177 isospin projections.

178 Considering all possible isospin projection pair configurations,

$$r^0 \equiv \sum_{\tau_{za} \leq \tau_{zb}} \sum_{i < j} (\delta_{\tau_{zi}, \tau_{za}} \delta_{\tau_{zj}, \tau_{zb}} + (1 - \delta_{\tau_{za}, \tau_{zb}}) \delta_{\tau_{zi}, \tau_{zb}} \delta_{\tau_{zj}, \tau_{za}}) = \sum_{i < j} \mathbf{1}, \quad (25)$$

179 where the identity is the same as in Eq. (15). The result of Eq. (25) is the total number of
180 nucleon pairs, $A(A-1)/2$, when evaluated within states of an A -nucleon system.

181 E. Square-separation operator

182 The expectation value of a square-separation operator describes the relative distance
183 squared of a pair of nucleons. The square-separation operator for a fixed pair of isospin
184 values and a fixed two-body total spin S can be defined as

$$r^2[S, \tau_{za}, \tau_{zb}] \equiv \sum_{i < j} (\vec{r}_i - \vec{r}_j)^2 [S] (\delta_{\tau_{zi}, \tau_{za}} \delta_{\tau_{zj}, \tau_{zb}} + (1 - \delta_{\tau_{za}, \tau_{zb}}) \delta_{\tau_{zi}, \tau_{zb}} \delta_{\tau_{zj}, \tau_{za}}). \quad (26)$$

185 Compared with (19) and (20), this is the same as setting

$$O(r) = r^2. \quad (27)$$

186 Summing over S in (26) gives

$$r^2[\tau_{za}, \tau_{zb}] \equiv \sum_{i < j} (\vec{r}_i - \vec{r}_j)^2 (\delta_{\tau_{zi}, \tau_{za}} \delta_{\tau_{zj}, \tau_{zb}} + (1 - \delta_{\tau_{za}, \tau_{zb}}) \delta_{\tau_{zi}, \tau_{zb}} \delta_{\tau_{zj}, \tau_{za}}). \quad (28)$$

187 The square-separation operator can be related to the relative mean-square-radius operator
188 [27, 28]

$$r_{\text{rel}}^2 = \frac{1}{A^2} \sum_{\tau_{za} \leq \tau_{zb}} r^2[\tau_{za}, \tau_{zb}], \quad (29)$$

189 which can be easily derived from

$$r_{\text{rel}}^2 \equiv \frac{1}{A} \sum_i (\vec{r}_i - \vec{R}_A)^2 \quad (30)$$

190 and

$$\vec{R}_A = \frac{1}{A} \sum_i \vec{r}_i. \quad (31)$$

191 It is convenient to define the relative mean-square-radius operator in each isospin projec-
192 tion pair sector (proton-proton, proton-neutron and neutron-neutron) [29],

$$\begin{aligned} r_{\text{rel},pp}^2 &\equiv \frac{1}{A^2} r^2\left[\frac{1}{2}, \frac{1}{2}\right], \\ r_{\text{rel},pn}^2 &\equiv \frac{1}{A^2} r^2\left[\frac{1}{2}, -\frac{1}{2}\right] = \frac{1}{A^2} r^2\left[-\frac{1}{2}, \frac{1}{2}\right], \\ r_{\text{rel},nn}^2 &\equiv \frac{1}{A^2} r^2\left[-\frac{1}{2}, -\frac{1}{2}\right]. \end{aligned} \quad (32)$$

193 The mean-square radius operators for protons and neutrons separately relative to the
 194 center of mass of all the nucleons are defined as [27]

$$r_p^2 \equiv \frac{1}{N_p} \sum_i \delta_{\tau_{zi}, \frac{1}{2}} (\vec{r}_i - \vec{R}_A)^2 \quad \text{and} \quad r_n^2 \equiv \frac{1}{N_n} \sum_i \delta_{\tau_{zi}, -\frac{1}{2}} (\vec{r}_i - \vec{R}_A)^2. \quad (33)$$

195 Substituting (31) into (33), it follows that [29]

$$\begin{aligned} r_p^2 &= \frac{2A - N_p}{N_p} r_{\text{rel},pp}^2 + \frac{A - N_p}{N_p} r_{\text{rel},pn}^2 - r_{\text{rel},nn}^2, \\ r_n^2 &= -r_{\text{rel},pp}^2 + \frac{A - N_n}{N_n} r_{\text{rel},pn}^2 + \frac{2A - N_n}{N_n} r_{\text{rel},nn}^2, \end{aligned} \quad (34)$$

196 where A , $N_p \equiv Z$ and $N_n \equiv N$ are nucleon, proton and neutron numbers, respectively. And
 197 $r_m \equiv \sqrt{r_{\text{rel}}^2}$, $r_p \equiv \sqrt{r_p^2}$ and $r_n \equiv \sqrt{r_n^2}$ are called the point-nucleon matter, point-proton and
 198 point-neutron rms radius, respectively. The relationship between them is

$$Ar_m^2 = N_p r_p^2 + N_n r_n^2. \quad (35)$$

199 F. Harmonic oscillator matrix elements

200 We can obtain the matrix elements of operators $O(r) = r^0$ and $O(r) = r^2$ in the convenient
 201 harmonic oscillator (HO) basis, noting that the angular parts of the wavefunctions are not
 202 effected so only matrix elements with $l = l'$ are non-zero,

$$\langle n'l' | r^0 | nl \rangle = \delta_{n,n'} \delta_{l,l'}, \quad (36)$$

203 and

$$\langle n'l' | r^2 | nl \rangle = b^2 \left[(2n + l + \frac{3}{2}) \delta_{n,n'} - \sqrt{n(n + l + \frac{1}{2})} \delta_{n,n'+1} - \sqrt{(n + 1)(n + l + \frac{3}{2})} \delta_{n,n'-1} \right] \delta_{l,l'}, \quad (37)$$

204 where $b \equiv \sqrt{\frac{\hbar}{\mu\Omega}}$ with $\mu = \frac{m_N}{2} = \frac{938.92 \text{ MeV}}{2c^2}$ (m_N is the average mass of a neutron and a
 205 proton with their mass given by PDG [30]) representing the reduced mass of a nucleon in
 206 the two-body subsystem. The derivation of these matrix elements has been detailed in the
 207 Appendix of Ref. [31].

208 We then take the additional step to transform these matrix elements from the relative
 209 center-of-mass frame to two-body matrix elements in the single-particle basis by the Moshin-
 210 sky transformation detailed in the Appendix. The resulting two-body matrix elements are
 211 then employed to calculate expectation values using many-body NCSM wavefunctions.

212 **III. *Ab-initio* NO CORE SHELL MODEL (NCSM) CALCULATION USING MFDn**

213 **A. Brief introduction of the calculation scheme**

214 In the *ab-initio* NCSM, we consider a system of point-like non-relativistic nucleons that
 215 interact by realistic inter-nucleon interactions. The NN or $NN + NNN$ interactions are
 216 taken from fitting NN phase shifts with high precision up to a certain energy and adjust-
 217 ing remaining parameters of the NNN interaction to a selection of 3-nucleon observables.
 218 Although we do not employ three-nucleon interactions [32–34], we plan to employ them in
 219 future studies that go beyond the scope of this work.

220 As the name NCSM implies, all the nucleons are considered active without an inert
 221 core that is assumed in standard, valence space, shell model calculations. The Hamiltonian
 222 operator for an A -nucleons system is thus

$$H_A = \sum_{i<j}^A \frac{(\vec{p}_i - \vec{p}_j)^2}{2m_N A} + \sum_{i<j}^A V_{ij} + \sum_{i<j<k}^A V_{ijk} + \dots \quad (38)$$

223 where V_{ij} is the two-body interaction, V_{ijk} is the three-body interaction, and so on.

224 We solve the eigenvalue problem

$$H_A |\Phi_A\rangle = E |\Phi_A\rangle \quad (39)$$

225 in the harmonic-oscillator (HO) basis with energy spacing between shells $\hbar\Omega$ and many-body
 226 truncation N_{\max} (the quanta of each shell is $N = 2n + l$, where n and l are the radial and
 227 orbital AM quantum numbers, respectively; N_{\max} defines the maximum total number of
 228 quanta allowed in the many-body basis states for this nucleus above the minimum required
 229 by the Pauli principle).

230 The calculations were carried out using MFDn (Many-Fermion Dynamics–nuclear), a con-
 231 figuration interaction (CI) code for nuclear structure calculations [35, 36]. It is a platform-
 232 independent Fortran 90 code using a hybrid MPI/OpenMP programming model, and is
 233 being used on current supercomputers, such as Cori and Perlmutter at NERSC, for *ab initio*
 234 calculations of atomic nuclei using realistic interactions. For recent applications of MFDn
 235 to the structure of light nuclei that includes three-nucleon interactions, see Refs. [37, 38].

236 B. Two-nucleon interaction

237 We adopt the Daejeon16 NN interaction [39] in our *ab initio* NCSM calculations. This
238 interaction is obtained by softening the chiral effective field theory (χ EFT) generated Idaho
239 next-to-next-to-next-to-leading order (N3LO) NN interaction using the similarity renor-
240 malization group (SRG) method [40, 41]. A special feature of this interaction is that it is
241 an NN interaction that attempts to absorb the effects of interactions that might otherwise
242 be treated as three and higher many-body forces, through phase-equivalent transformations
243 (PETs) [42]. The optimal set of PET parameters are obtained by fitting the binding energies
244 and spectra of selected light nuclei up to ^{16}O . The Daejeon16 interaction provides a good
245 convergence rate in *ab initio* calculations for light nuclei compared with other realistic inter-
246 actions [43, 44]. Ground state energies and radii calculated using this interaction are in good
247 agreement with the results of experiments for p -shell nuclei [45]. Recently, the applications
248 of Daejeon16 have been extended to medium and heavy nuclei [46] using a mean-field with
249 the inclusion of a phenomenological 3-body contact interaction.

250 In addition, the Daejeon16 interaction has found many applications in scattering and
251 resonances using the single-state HO representation of scattering equations (SS-HORSE)
252 method [47–51]. Artificial Neural Networks (ANN) were explored as a new extrapolation
253 tool for *ab initio* NCSM calculation using the Daejeon16 interaction [52].

254 The construction of the Daejeon16 interaction is charge/isospin independent, so the
255 Coulomb interaction between protons is added in our calculations.

256 C. Parameter Setting

257 We selected $N_{\text{max}} = 16$ for the many-nucleon basis space cutoff and $\hbar\Omega = 10$ MeV for
258 the HO energy spacing in the *ab initio* NCSM calculation. $N_{\text{max}} = 16$ is chosen because
259 this is the N_{max} value sufficient for our demonstration goals and reasonable in terms of
260 total computational resources needed. $\hbar\Omega = 10$ MeV was found to provide approximate
261 N_{max} independence for the point-nucleon rms radii r_p , r_n and r_m as seen in Fig. 1 and
262 Fig. 2. Then, by comparing the rms radii at $\hbar\Omega = 10$ MeV from $N_{\text{max}} = 18$ with those
263 from $N_{\text{max}} = 16$, we can make a rough estimation of the uncertainty in these results. As
264 detailed in Fig. 2, the resulting estimated uncertainty of point-nucleon rms radii due to basis

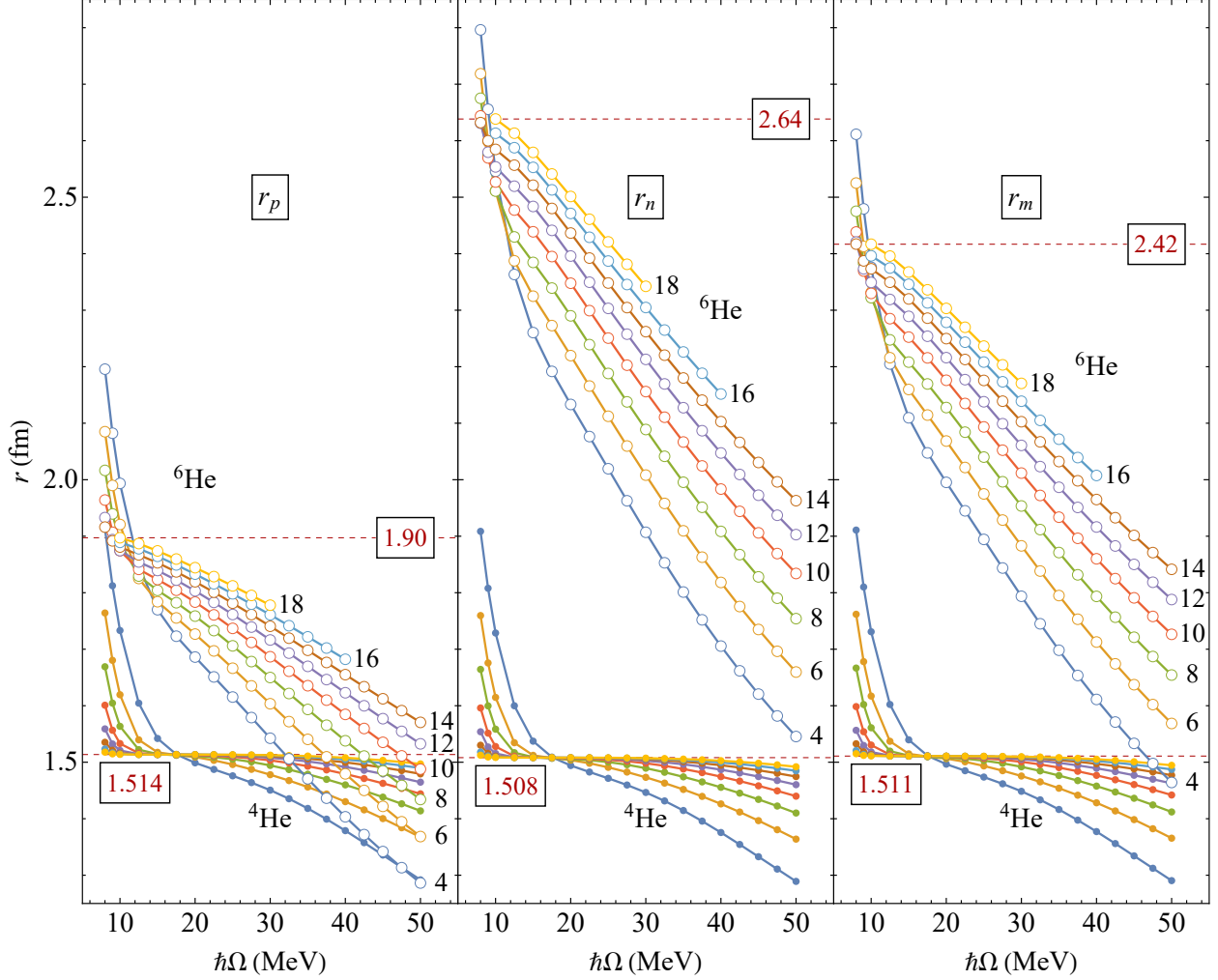


FIG. 1. r_p , r_n and r_m of ${}^4\text{He}$ and ${}^6\text{He}$ with Daejeon16 interaction plus Coulomb potential, calculated by MFDn for *ab initio* NCSM. Results for ${}^4\text{He}$ (${}^6\text{He}$) are represented by filled (open) circles, which are connected by a sequence of straight lines for the same N_{max} . The N_{max} values for ${}^6\text{He}$ are shown on the right of the sequences of lines, and the color used to label each N_{max} for ${}^4\text{He}$ is the same as ${}^6\text{He}$. The horizontal red dashed lines with numbers in rectangle boxes indicate the $r_{p/n/m}$ values for $N_{\text{max}} = 18$ with $\hbar\Omega$ corresponding to the minimum gap between the calculated points for $N_{\text{max}} = 18$ and $N_{\text{max}} = 16$ (i.e., the minimum $|\Delta r|$ in Fig. 2).

265 truncation $N_{\text{max}} = 16$ at $\hbar\Omega = 10$ MeV is about 0.03 fm for ${}^6\text{He}$ and 0.001 fm for ${}^4\text{He}$. In
 266 addition, we set the maximum total AM of the interaction between nucleons at $J_{\text{max}} = 6$
 267 for the Daejeon16 interaction. Since the NN interactions are short-range interactions, and
 268 we are interested in only the ground states of these light nuclei, contributions from larger
 269 values of J to the expectation value of $O(r)$ are anticipated to be vanishingly small.

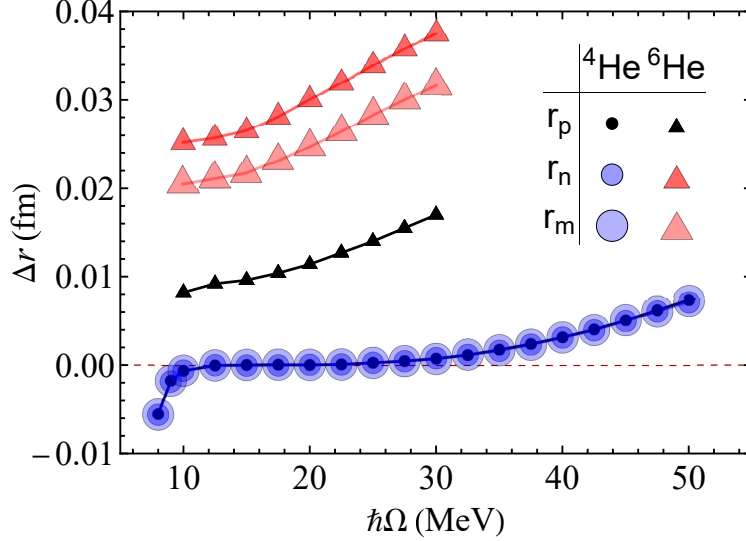


FIG. 2. Δr obtained by subtracting $r_{p/n/m}$ for $N_{\max} = 18$ from those for $N_{\max} = 16$. The absolute value $|\Delta r|$ serves as an indicator of the major source of uncertainty of $r_{p/n/m}$ for ${}^4\text{He}$ and ${}^6\text{He}$ at $N_{\max} = 16$ in the *ab initio* NCSM calculation.

270 IV. RESULTS AND ANALYSIS

271 A. The expectation value of pair-identity operator

TABLE I. Results of $\langle r^0[S, \tau_{za}, \tau_{zb}] \rangle$ for ${}^4\text{He}$ and ${}^6\text{He}$ ($\hbar\Omega = 10$ MeV, $N_{\max} = 16$), with the Daejeon16 interaction plus Coulomb potential, using MFDn with accuracy of 5 significant digits (to display in a uniform format, 6 decimal digits are shown across the calculated columns). The “expected” value (exp.) of each calculated result (cal.), based on occupying only the lowest available states in a HO basis, is listed for comparison as discussed in the text. The sum of each column is shown in the last line, which is equal to the number of pairs $A(A - 1)/2$ for each nucleus.

S	${}^4\text{He}$ exp.	${}^4\text{He}$ cal.	${}^6\text{He}$ exp.	${}^6\text{He}$ cal.
<i>pp</i> 0	~ 1	0.976772	~ 1	0.967578
<i>pp</i> 1	~ 0	0.023228	~ 0	0.032422
<i>np</i> 0	~ 1	0.979111	~ 2	1.977430
<i>np</i> 1	~ 3	3.020890	~ 6	6.022570
<i>nn</i> 0	~ 1	0.976774	~ 3	2.865420
<i>nn</i> 1	~ 0	0.023226	~ 3	3.134580
#pairs	6	6.000001	15	15.00000

272 $\langle r^0[S, \tau_{za}, \tau_{zb}] \rangle$ provides the probability of finding a nucleon pair with fixed two-body total

273 spin S and a given pair of isospin projections $\{\tau_{za}, \tau_{zb}\}$. We begin with analyzing the results
 274 of $\langle r^0[S, \tau_{za}, \tau_{zb}] \rangle$ for both values of S and for the $\{\tau_{za}, \tau_{zb}\}$ combinations shown in Table I.

275 We first check the sum of all $\langle r^0[S, \tau_{za}, \tau_{zb}] \rangle$ values for ${}^4\text{He}$ and ${}^6\text{He}$ in the last row of
 276 Table I and confirm that they are equal to the total number of nucleon pairs $A(A-1)/2$ for
 277 each nucleus (Eq. (25)) within 5 significant digits. We also check the sums of $\langle r^0[S, \tau_{za}, \tau_{zb}] \rangle$
 278 over two-body total spin S , $\langle r^0[\tau_{za}, \tau_{zb}] \rangle = \sum_S \langle r^0[S, \tau_{za}, \tau_{zb}] \rangle$, and confirm that they are
 279 equal to the integer number of pairs with given $\{\tau_{za}, \tau_{zb}\}$ in ${}^4\text{He}$ and ${}^6\text{He}$ (Eq. (24)) within
 280 5 significant digits.

281 We expect and find that pp and nn pairs in the ground state of ${}^4\text{He}$ are dominantly
 282 spin-singlet, because this is the only $l = 0$ basis state (s -state) respecting the overall an-
 283 tisymmetrization for exchanging of two isospin-symmetric fermions, i.e. $(-1)^{l+S+T} = -1$,
 284 where l , S and T are the two-body relative orbital AM, two-body total spin and two-body
 285 total isospin. One may expect, as we indeed find, a small but non-zero portion of triplet
 286 arising from partial wave contributions at higher values of l .

287 The added Coulomb potential makes the isospin symmetry only approximate in our
 288 calculations (note that we assume equal mass for the p and the n which is taken as the average
 289 mass of these nucleons and Daejeon16 is charge-independent), which will contribute to the
 290 difference of expectation values between pp and nn pairs. However, this deviation should
 291 be small and consistent with the fact that isospin is known to be a very good symmetry for
 292 light nuclei.

293 For the spin-independent parts of the NN interactions, singlet and triplet states have the
 294 same energy in the same HO wave function of relative motion (labeled by n and l for two-
 295 body central potentials)—there is no preference between the allowed spin configurations.
 296 When the probabilities are interpreted in a pictorial way, we can let each np pair in the
 297 ground state's dominant configuration take one of the possible spin configurations $\uparrow\uparrow$, $\downarrow\downarrow$,
 298 $\uparrow\downarrow + \downarrow\uparrow$ and $\uparrow\downarrow - \downarrow\uparrow$, as illustrated for ${}^4\text{He}$ in the left of Fig. 3. Upon considering the
 299 spin-dependent part of the NN potential, e.g. $S_p S_n$ coupling in the s -state, which can be
 300 usefully written as $V_{\text{spin}} = \frac{1}{\hbar^2} V_1(r) \vec{S}_p \cdot \vec{S}_n$ [53], the probability of finding an np pair in one of
 301 the triplet states can be slightly larger than in the singlet state if $V_1(r)$ is effectively attractive
 302 (thus negative), as in deuterium. This assessment takes into account that $\langle \vec{S}_p \cdot \vec{S}_n \rangle = +\hbar^2/4$
 303 for triplet and $-3\hbar^2/4$ for singlet. All these expectations are met, as can be seen in the
 304 calculated results in Table I.

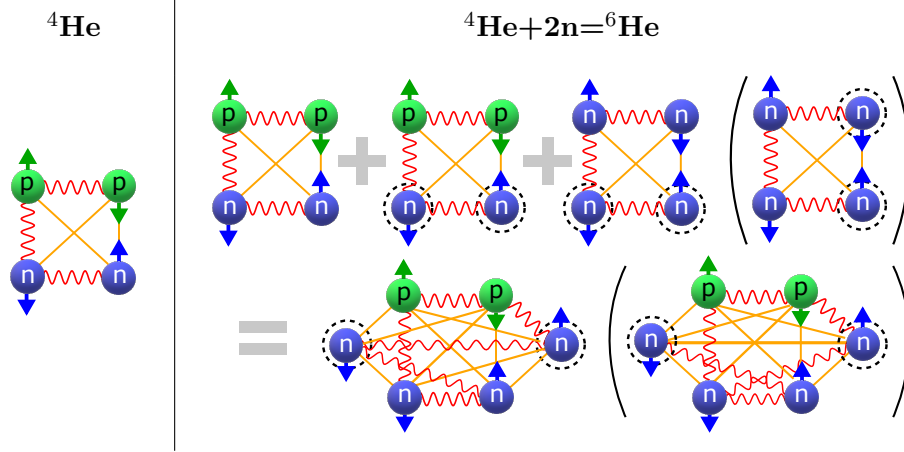


FIG. 3. A schematic view of the expected ground state dominant two-body total spin configuration for ${}^4\text{He}$ (left) and ${}^6\text{He}$ (right). The spin projections are indicated by arrows. The red wavy line (orange straight line) indicates a pair with two-body total spin $S = 0$ ($S = 1$). The right side shows the process of constructing a ${}^6\text{He}$ nucleus from ${}^4\text{He}$ and two additional neutrons (specified by dashed circles), if the ${}^4\text{He}$ two-body total spin configuration is preserved inside the ${}^6\text{He}$ nucleus. The ${}^6\text{He}$ configuration can be constructed by combining three partial configurations. The first part is the same configuration inherited from ${}^4\text{He}$, and the second (third) part is the configuration formed by the “core” protons (“core” neutrons) and the valence neutrons. The resulting configuration of ${}^6\text{He}$ is shown on the second row. The configuration in the bracket shows another possible configuration which will be discussed in the text.

305 A pictorial illustration of the process of forming the dominant two-body total spin con-
 306 figuration for ${}^6\text{He}$ is shown in the right panel of Fig. 3. In this idealization, we follow a
 307 simple viewpoint by assuming that the two-body total spin configuration of the “ α core” of
 308 ${}^6\text{He}$ is the same as ${}^4\text{He}$ due to the stable closed-shell structure of ${}^4\text{He}$. We further assume
 309 the same set of two-body total spins for the four {valence neutron, proton} pairs as for the
 310 four {“ α core” neutron, proton} pairs, because the probability of each pair to pick up the
 311 four configurations $\uparrow\uparrow$, $\downarrow\downarrow$, $\uparrow\downarrow + \downarrow\uparrow$ and $\uparrow\downarrow - \downarrow\uparrow$ might reasonably be assumed to remain
 312 roughly the same. Following the same line of reasoning, the four {valence neutron, “ α core”
 313 neutron} pairs also pick up these four configurations with approximately equal probabilities.
 314 Naturally, the neutron pair of the core is assumed to take the same spin singlet configura-
 315 tion as the proton pair. After these assumptions, the only two-body total spin left to be
 316 determined is the one for the pair of the two valence neutrons. We inspect Table I and find

317 that if we take this valence pair to be **singlet**, all the calculated $\langle r^0[S, \tau_{za}, \tau_{zb}] \rangle$ match our
 318 expectations, and the maximum value they deviate from their corresponding exact integer
 319 values is 0.14, which is small on these scales. The dominance of singlet state over triplet
 320 state in the valence pair has also been seen in Ref. [54, 55]. That the $\langle r^0[S, \tau_{za}, \tau_{zb}] \rangle$ val-
 321 ues are non-integers can be understood as arising from non-dominant configurations in the
 322 ground state. In addition, as mentioned above, the Coulomb effect plays a small role in the
 323 observed differences between results of pp and nn . It is interesting to note that when we
 324 exclude ${}^6\text{He}$ nn pairs, the largest deviation between any calculated result and its nearest
 325 “expected” integer number is only 0.033 for ${}^6\text{He}$ and 0.024 for ${}^4\text{He}$. This is consistent with
 326 our assumption that the two valence neutrons have a small influence on the “ α core” spin
 327 configurations.

328 Another possible ${}^6\text{He}$ two-body total spin configuration is shown in the bracket of Fig. 3,
 329 where the two valence neutrons form a triplet spin state. We note that the two valence
 330 neutrons in this case are symmetrical with respect to the “core” neutrons. However, the
 331 total number of singlet (triplet) spin states formed by each nucleon with other nucleons varies
 332 from one nucleon to another. On the contrary, in the previously discussed configuration,
 333 each nucleon forms two singlet and three triplet spin states with the other nucleons. As a
 334 whole, the unbracketed configuration is more symmetrical than the bracketed configuration.
 335 So from the symmetry point of view, the unbracketed configuration appears to be a more
 336 natural choice.

337 We now address the role of N_{max} truncation. The maximum difference of $\langle r^0[S, \tau_{za}, \tau_{zb}] \rangle$
 338 between $N_{\text{max}} = 16$ and $N_{\text{max}} = 14$ is 1×10^{-4} for ${}^6\text{He}$ pp/pn pairs and 5×10^{-4} for ${}^6\text{He}$
 339 nn pairs. Keeping in mind that the MFDn calculation preserves 5 significant digits, it is
 340 meaningful that the dependence on basis truncation still resides in the 4th decimal digit of
 341 the results. On the other hand, for ${}^4\text{He}$, the maximum difference of $\langle r^0[S, \tau_{za}, \tau_{zb}] \rangle$ between
 342 $N_{\text{max}} = 16$ and $N_{\text{max}} = 14$ is 4×10^{-5} , so the uncertainty due to truncation that we quote
 343 only appears in the 5th decimal digit.

344 We further examine the major components (labeled by the spectroscopy symbol $n^{2S+1}l_J$,
 345 where $|l - S| \leq J \leq |l + S|$) of the three isospin-projected pair configurations, as shown in
 346 Fig. 4. For ${}^4\text{He}$, all the major components are in the s -state, as expected. pp is mostly (81%)
 347 in the lowest singlet state, with a small portion (12%) in the $n = 1$ singlet s -state. The pp
 348 components of ${}^6\text{He}$ are almost identical to that of ${}^4\text{He}$. The triplet states of np for ${}^4\text{He}$ are

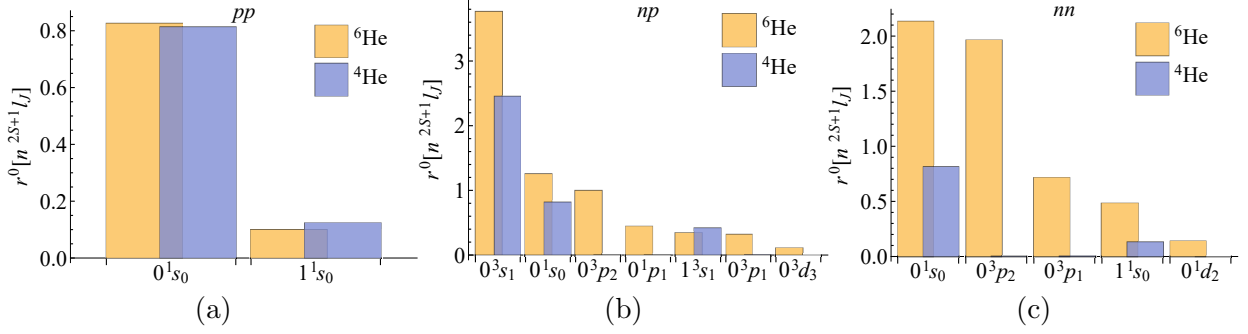


FIG. 4. Major components of the pp (a), np (b) and nn (c) pair configurations of ${}^4\text{He}$ and ${}^6\text{He}$ for $N_{\text{max}} = 16$ and $\hbar\Omega = 10$ MeV. The bins are arranged in decreasing order for ${}^6\text{He}$, with the corresponding ${}^4\text{He}$ bins shown side by side for comparison. The above shown components in total comprises more than 90% of $\langle r^0 \rangle$ in each isospin-projected pair configuration.

349 dominated by the s -state's lowest two components ($n = 0$ and $n = 1$), while np singlet is
350 dominantly (81%) in the lowest s -state. For ${}^6\text{He}$ np pairs, we see the rising of p/d -states (22%
351 for the three major p -states in total and 1% for the 0^3d_3 state), contributing to both singlet
352 and triplet states. For the nn case, we again see the rising of higher-state components (45%
353 p and 2% d) in ${}^6\text{He}$, compared with ${}^4\text{He}$. However, due to the $(-1)^{l+S+T} = -1$ antisymmetry
354 constraint, the allowed p -states are triplet and the allowed s/d -states are singlet. It follows
355 that, for ${}^6\text{He}$, nn triplets are dominantly in p -states and nn singlets are dominantly in
356 s -states.

357 To sum up, we estimate that the two ${}^6\text{He}$ valence neutrons dominantly form a **singlet** spin
358 configuration and mostly in an s -state from the consideration of preserving ${}^4\text{He}$ two-body
359 total spin configuration inside ${}^6\text{He}$ (which can be suggested by the fact that pp components
360 stay almost unchanged in Fig. 4), respecting the overall symmetry in forming triplets and
361 singlets (for example, each nucleon in ${}^6\text{He}$ forms two singlets and three triplets with the other
362 nucleons, as can be seen in Fig. 3), and consistency with the *ab initio* NCSM calculated r^0
363 moments (Table I and Fig. 4). This provides an indicator of halo structure in ${}^6\text{He}$ through
364 the following reasoning. The nn singlet s -state has a symmetric spatial wave function Ψ_{nlm}
365 which has non-zero probability close to the center of mass of the pair due to the absence of
366 a centrifugal term in the relative Schrödinger equation, resulting in a stronger correlation
367 compared with triplet states, which seems to support a “di-neutron” halo at some distance
368 from the center of mass of the nucleus. The “cigar”-like configuration is another possibility

369 seen in many calculations but appears not to be the dominant configuration [1, 54, 55].

370 It is clear from our discussion above that the determination of the dominant two-body
 371 total spin configuration from the simple analysis of $\langle r^0[S, \tau_{za}, \tau_{zb}] \rangle$ involves many assump-
 372 tions. To reduce those assumptions, we need to know to what extent the ${}^4\text{He}$ two-body
 373 total spin configuration is preserved inside ${}^6\text{He}$. Furthermore, the equal chance of picking
 374 the four possible two-body spin configurations is based on symmetry assumptions between
 375 isospin-symmetric pairs. We need to know to what extent these symmetry assumptions
 376 apply. After the following analysis of $\langle r^2[S, \tau_{za}, \tau_{zb}] \rangle$, instead of guessing the two-body total
 377 spin configuration, we will develop a method of building classical static 3D models, first
 378 analytically then numerically employing results from our *ab initio* NCSM calculations. The
 379 analytical models still involve symmetry assumptions, while the numerical models allow us
 380 to partially remove these assumptions and yielding a model that is more data-driven.

381 B. The expectation value of square-separation operator

TABLE II. Results of $\langle r^2[S, \tau_{za}, \tau_{zb}] \rangle$ for ${}^4\text{He}$ and ${}^6\text{He}$ ($\hbar\Omega = 10$ MeV, $N_{\text{max}} = 16$), with the Daejeon16 interaction plus Coulomb potential, using MFDn with accuracy of 5 significant digits. We also present in the second (third) column of each nucleus the mean squared separation (rms separation) of given $\{S, \tau_{za}, \tau_{zb}\}$ defined in the text. The last line shows the sum of $\langle r^2[S, \tau_{za}, \tau_{zb}] \rangle$ for each nucleus.

S	${}^4\text{He}$			${}^6\text{He}$		
	$\langle r^2 \rangle [\text{fm}^2]$	$\overline{\langle r^2 \rangle} [\text{fm}^2]$	$\overline{\langle r^2 \rangle}^{1/2} [\text{fm}]$	$\langle r^2 \rangle [\text{fm}^2]$	$\overline{\langle r^2 \rangle} [\text{fm}^2]$	$\overline{\langle r^2 \rangle}^{1/2} [\text{fm}]$
<i>pp</i> 0	5.95862	6.10032	2.46988	6.63201	6.85424	2.61806
<i>pp</i> 1	0.22754	9.79581	3.12983	0.36145	11.1484	3.33892
<i>np</i> 0	5.94563	6.07248	2.46424	24.5046	12.3921	3.52024
<i>np</i> 1	18.3172	6.06352	2.46242	73.2384	12.1607	3.48721
<i>nn</i> 0	5.89396	6.03411	2.45644	38.7177	13.5121	3.67588
<i>nn</i> 1	0.22648	9.75110	3.12268	63.2643	20.1827	4.49252
sum	36.5695	-	-	206.718	-	-

382 To obtain a normalization of $\langle r^2[S, \tau_{za}, \tau_{zb}] \rangle$ useful for developing a classical picture, we
 383 define the mean squared separation between two nucleons of given $\{S, \tau_{za}, \tau_{zb}\}$ as

$$\overline{\langle r^2[S, \tau_{za}, \tau_{zb}] \rangle} \equiv \frac{\langle r^2[S, \tau_{za}, \tau_{zb}] \rangle}{\langle r^0[S, \tau_{za}, \tau_{zb}] \rangle}, \quad (40)$$

384 and the rms separation of given $\{S, \tau_{za}, \tau_{zb}\}$

$$\overline{\langle r^2[S, \tau_{za}, \tau_{zb}] \rangle}^{1/2} \equiv \sqrt{\frac{\langle r^2[S, \tau_{za}, \tau_{zb}] \rangle}{\langle r^0[S, \tau_{za}, \tau_{zb}] \rangle}}. \quad (41)$$

385 The derived quantities defined by (40) and (41) are shown in the last two columns of
 386 Table II for ${}^4\text{He}$ and ${}^6\text{He}$, along with the original *ab initio* NCSM results in the first column
 387 for each nucleus. These results can be interpreted with the following considerations. Using
 388 again the overall antisymmetrization property of fermion pairs as mentioned in Sec. IV A,
 389 the rms separation for singlet is expected to be smaller than triplet for the *pp* and *nn* pairs in
 390 their lowest partial waves. This is true for both ${}^4\text{He}$ (2.5 fm versus 3.1 fm) and ${}^6\text{He}$ (2.6 fm
 391 versus 3.3 fm for *pp*; 3.7 fm versus 4.5 fm for *nn*) seen in Table II. For *np* pairs, since the
 392 total two-body isospin T can be either 0 or 1, the spatial part of the wave function for given
 393 S can be either symmetric or antisymmetric. Thus, the rms separation for singlet *np* pairs
 394 and triplet *np* pairs are similar (~ 2.46 fm for both in ${}^4\text{He}$; 3.52 fm versus ~ 3.49 fm in ${}^6\text{He}$).

395 Comparing ${}^4\text{He}$ and ${}^6\text{He}$, we see that the rms separation for *pp* singlet configuration,
 396 which is the dominant two-body spin configuration of *pp*, is expanded by 6% from ${}^4\text{He}$
 397 to ${}^6\text{He}$. Interestingly, the remaining $\sim 3\%$ (from Table I) portion of *pp* triplet state also
 398 experiences a similar expansion from ${}^4\text{He}$ to ${}^6\text{He}$. On the other hand, the rms separation for
 399 *nn* and *np* pairs are expanded by 40%~50% from ${}^4\text{He}$ to ${}^6\text{He}$.

400 Independent of S , we define the mean squared separation for nucleon pairs of given
 401 $\{\tau_{za}, \tau_{zb}\}$ as

$$\overline{\langle r^2[\tau_{za}, \tau_{zb}] \rangle} \equiv \frac{\sum_S \langle r^2[S, \tau_{za}, \tau_{zb}] \rangle}{\sum_S \langle r^0[S, \tau_{za}, \tau_{zb}] \rangle} = \frac{\langle r^2[\tau_{za}, \tau_{zb}] \rangle}{\#\text{pairs}[\tau_{za}, \tau_{zb}]}, \quad (42)$$

402 where we use $\#\text{pairs}[\tau_{za}, \tau_{zb}]$ to indicate that this is an integer number that represents the
 403 number of pairs of given $\{\tau_{za}, \tau_{zb}\}$, according to the sum rule (24). The rms separation of
 404 given $\{\tau_{za}, \tau_{zb}\}$ can be defined as the square root of the above quantity. The results are
 405 shown in Table III.

406 We can also calculate the mean squared separation of an arbitrary pair in a nucleus

$$\overline{\langle r^2 \rangle}_A \equiv \frac{\sum_{S, \tau_{za} \leq \tau_{zb}} \langle r^2[S, \tau_{za}, \tau_{zb}] \rangle}{\sum_{S, \tau_{za} \leq \tau_{zb}} \langle r^0[S, \tau_{za}, \tau_{zb}] \rangle} = \frac{\langle r^2 \rangle}{A(A-1)/2}, \quad (43)$$

407 where we have used the sum rule (25). The square root of the quantity in (43) characterizes
 408 the rms nucleon-nucleon separation within a nucleus.

TABLE III. $\langle r^2[\tau_{za}, \tau_{zb}] \rangle$ calculated from Table II, along with the mean squared separation and rms separation for nucleon pairs of given $\{\tau_{za}, \tau_{zb}\}$.

	${}^4\text{He}$			${}^6\text{He}$		
	$\langle r^2 \rangle [\text{fm}^2]$	$\langle r^2 \rangle [\text{fm}^2]$	$\langle r^2 \rangle^{1/2} [\text{fm}]$	$\langle r^2 \rangle [\text{fm}^2]$	$\langle r^2 \rangle [\text{fm}^2]$	$\langle r^2 \rangle^{1/2} [\text{fm}]$
<i>pp</i>	6.18616	6.18616	2.48720	6.99346	6.99346	2.64452
<i>np</i>	24.2629	6.06572	2.46287	97.7429	12.2179	3.49541
<i>nn</i>	6.12044	6.12044	2.47395	101.982	16.9970	4.12274

409 Using (43) with the data of Table II, we get $\overline{\langle r^2 \rangle}_{4\text{He}} = 6.0949$ ($\overline{\langle r^2 \rangle}_{6\text{He}} = 13.781$) fm^2 and
410 $\overline{\langle r^2 \rangle}_{4\text{He}}^{1/2} = 2.4688$ ($\overline{\langle r^2 \rangle}_{6\text{He}}^{1/2} = 3.7123$) fm . This indicates that the nucleon-nucleon separations
411 of ${}^6\text{He}$, on average, are 50% greater than those of ${}^4\text{He}$.

412 Traditionally, we can also calculate the rms radii of point-nucleon proton, neutron and
413 matter distributions relative to the center of mass of the nucleus, $\langle r_p^2 \rangle^{1/2}$, $\langle r_n^2 \rangle^{1/2}$ and
414 $\langle r_m^2 \rangle^{1/2} = \langle r_{\text{rel}}^2 \rangle^{1/2}$, using (32), (34) and (29). These results are shown in Table IV. The
415 point-proton rms radius increases by $\sim 25\%$ from ${}^4\text{He}$ ($r_p = 1.515$ fm) to ${}^6\text{He}$ ($r_p = 1.889$ fm).
416 This increase may be understood as a consequence of halo structure, arising from the motion
417 of the charged α core around the common center of mass as well as possible contributions
418 from swelling of the α core [56].

TABLE IV. Mean squared radii $\langle r_p^2 \rangle$, $\langle r_n^2 \rangle$ and $\langle r_m^2 \rangle$, along with the rms radii $r_p = \langle r_p^2 \rangle^{1/2}$, $r_n = \langle r_n^2 \rangle^{1/2}$ and $r_m = \langle r_m^2 \rangle^{1/2}$ for ${}^4\text{He}$ and ${}^6\text{He}$ ($\hbar\Omega = 10$ MeV , $N_{\text{max}} = 16$).

<i>x</i>	${}^4\text{He}$		${}^6\text{He}$	
	$\langle r_x^2 \rangle [\text{fm}^2]$	$\langle r_x^2 \rangle^{1/2} [\text{fm}]$	$\langle r_x^2 \rangle [\text{fm}^2]$	$\langle r_x^2 \rangle^{1/2} [\text{fm}]$
<i>p</i>	2.29381	1.51453	3.56864	1.88908
<i>n</i>	2.27738	1.50910	6.82895	2.61323
<i>m</i>	2.28559	1.51182	5.74218	2.39628

419 According to Table IV, the ${}^4\text{He}$ rms radii of protons and neutrons are nearly the same,
420 about $r_0 = 1.51$ fm . And from Table III, we see that the rms separation of *pp*, *np* and
421 *nn* are also very similar, about $a = 2.47$ fm . The ratio $a/r_0 = 1.636$ is similar to the
422 $\frac{\text{side length}}{\text{center-to-vertex distance}}$ ratio of a tetrahedron $\frac{2\sqrt{6}}{3} \approx 1.633$. This suggests a route by
423 which we can relate our quantum many-body results to a classical picture that depicts ${}^4\text{He}$
424 as a tetrahedron with protons and neutrons being at the tetrahedron's vertices.

425 The analysis for ${}^6\text{He}$ is more complicated. In Table III, we see that the *pp* rms separation
426 of ${}^6\text{He}$ increases by 6.3%, while the *np* (*nn*) rms separation of ${}^6\text{He}$ increases by 41.9%

427 (66.6%), compared with those of ${}^4\text{He}$. Even before detailed analysis, this can be interpreted
 428 by a simple binary picture. Assuming the rms separation for nucleon pairs formed by the
 429 “ α core” nucleons in ${}^6\text{He}$ is distinct from the rms separation for the remaining ${}^6\text{He}$ nucleon
 430 pairs, with

$$\frac{r_{np/nn,i}^{(6\text{He})}}{r_{np/nn}^{(4\text{He})}} = \begin{cases} x, & \text{nucleon pair } i \text{ belongs to the “}\alpha \text{ core”} \\ y, & \text{otherwise} \end{cases}, \quad (44)$$

431 we can match the np and nn rms separation percentage increases by setting

$$\frac{r_{np}^{(6\text{He})} - r_{np}^{(4\text{He})}}{r_{np}^{(4\text{He})}} = \sqrt{\frac{4x^2 + 4y^2}{8}} - 1 = 41.9\%, \quad (45)$$

432 and

$$\frac{r_{nn}^{(6\text{He})} - r_{nn}^{(4\text{He})}}{r_{nn}^{(4\text{He})}} = \sqrt{\frac{x^2 + 5y^2}{6}} - 1 = 66.6\%, \quad (46)$$

433 where we have used $r_{np} = \langle r_{np}^2 \rangle^{1/2}$ and $r_{nn} = \langle r_{nn}^2 \rangle^{1/2}$. The results are $x = 0.93$ and $y = 1.78$,
 434 i.e. the np/nn rms separation for the core stays nearly the same as the one for ${}^4\text{He}$. At
 435 the same time the np/nn rms separation for pairs not belonging to the core are found to
 436 increase by almost 80%, indicating the formation of a halo. However, this simple binary
 437 model treats the “ α core” as approximately a point mass when viewed by each of the two
 438 valence neutrons, ignoring the fact that the size of the “ α core” is comparable to the distance
 439 between the valence neutrons and the core.

440 One can also infer the ${}^6\text{He}$ structure in the momentum space. Our calculated binding
 441 energy of ${}^4\text{He}$ (${}^6\text{He}$) is -28.3597 (-29.3387) MeV for $N_{\text{max}} = 16$ and $\hbar\omega = 10$ MeV, so the
 442 two-neutron separation energy for ${}^6\text{He}$ is $s = 0.979$ MeV. The characteristic wave number
 443 k_{ch} associated with this energy scales as $\sqrt{sm_N/\hbar^2}$, which gives $k_{\text{ch}} \sim 0.15 \text{ fm}^{-1}$ (relative
 444 distance ~ 6.5 fm). This k_{ch} (relative distance) is quite separated from that of the ${}^4\text{He}$
 445 “core”, which is $\sim 0.7 \text{ fm}^{-1}$ (~ 1.4 fm). However, this simple expression only accounts for
 446 the s -states. As can be seen in Fig. 4, p/d -states also play an important role in nn and np
 447 pairs of ${}^6\text{He}$.

448 V. 3D MODELING

449 Although the atomic nucleus is a quantum mechanical object, and the position of each
 450 nucleon cannot be fixed in space, we can assume that among all the possible relative position

451 configurations, there is one dominating at the ground state. Another way to put it is that
 452 we can imagine making a sequence of snapshots of the nucleus at a sequence of moments
 453 in time, and it will turn out that there is one particular relative position configuration that
 454 we have the highest probability of finding. Based on this scenario, we make a static and
 455 classical assumption which enables us to build a 3D model of relative positions for nucleons
 456 in a nucleus using our *ab initio* calculations as inputs.

457 A. A simple analytic model independent of spin considerations

We build our 3D analytic model of ${}^6\text{He}$ by adding two neutrons to the tetrahedron “ α core” discussed above. We preserve the geometric symmetry as much as possible in this model. The geometry of this model is shown in Fig. 5. The four vertices of the tetrahedron represent the four “ α core” nucleons in ${}^6\text{He}$, which are labeled as A , B , C and D . The center of the tetrahedron is placed at the origin. The distance from any of the tetrahedron vertices to the center of tetrahedron is r_0 . The other two neutrons are labeled as E and F . The perpendicular bisector of EF connecting to the center of the tetrahedron also perpendicular bisects AB . This arrangement limits the locations of the other two neutrons to a plane defined by C , D and the center of the tetrahedron, as illustrated in Fig. 5. We note that in a tetrahedron structure, any line connecting two arbitrary vertices is perpendicular to the line connecting the remaining two vertices. The two neutrons outside the tetrahedron therefore cannot be equidistant from all of the four “ α core” nucleons. We can at most have equidistance from two of the “ α core” nucleons. In other words, in Fig. 5, $EA = EB = FA = FB$, but $ED = FC \neq (<)EC = FD$. In reference to Fig. 5, we can adopt the nucleon coordinates $A(\frac{2\sqrt{2}}{3}r_0, 0, -\frac{1}{3}r_0)$, $B(0, 0, r_0)$, $C(-\frac{\sqrt{2}}{3}r_0, \frac{\sqrt{6}}{3}r_0, -\frac{1}{3}r_0)$, $D(-\frac{\sqrt{2}}{3}r_0, -\frac{\sqrt{6}}{3}r_0, -\frac{1}{3}r_0)$, $E(x, -w, \frac{\sqrt{2}}{2}x)$ and $F(x, w, \frac{\sqrt{2}}{2}x)$ with adjustable parameters x and w . The squared separations are thus parametrized as

$$\begin{aligned}
 |EA|^2 &= |EB|^2 = |FA|^2 = |FB|^2 = (x - \frac{2\sqrt{2}}{3}r_0)^2 + w^2 + (\frac{\sqrt{2}}{2}x + \frac{r_0}{3})^2, \\
 |EC|^2 &= |FD|^2 = (x + \frac{\sqrt{2}}{3}r_0)^2 + (w + \frac{\sqrt{6}}{3}r_0)^2 + (\frac{\sqrt{2}}{2}x + \frac{r_0}{3})^2, \\
 |ED|^2 &= |FC|^2 = (x + \frac{\sqrt{2}}{3}r_0)^2 + (w - \frac{\sqrt{6}}{3}r_0)^2 + (\frac{\sqrt{2}}{2}x + \frac{r_0}{3})^2, \\
 |EF|^2 &= 4w^2.
 \end{aligned}
 \tag{47}$$

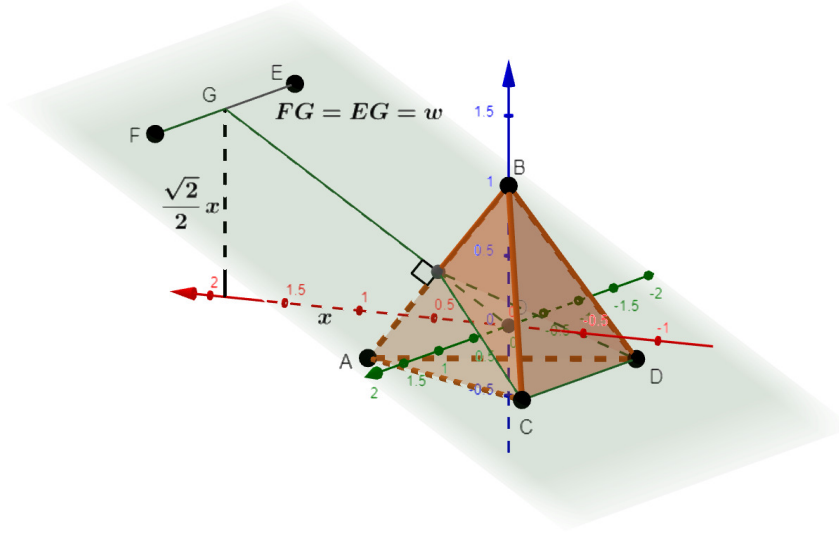


FIG. 5. The analytic model of ${}^6\text{He}$ parametrized by x and w . The origin is set at the center of the tetrahedron. EF is parallel to CD and perpendicular to AB . In this model, $EA = EB = FA = FB$, $ED = FC$ and $EC = FD$. The scale of the axes is in units of r_0 , which is the distance from the center of the tetrahedron to any of the four vertices. The green tilted plane contains the added two neutrons whose locations define the model parameters x and w . We note that x can be positive or negative or 0, while $w = FG = EG$ can only be positive.

To connect this model with the *ab initio* calculation results of Table III, we introduce

$$r_{np}^{\prime 2} = \left(\langle r_{np}^2 \rangle^{(6\text{He})} - \langle r_{np}^2 \rangle^{(4\text{He})} \right) / 4 \quad \text{and} \quad b = \langle r_{nn}^2 \rangle^{(6\text{He})} - \langle r_{nn}^2 \rangle^{(4\text{He})}, \quad (48)$$

458 which are $73.4800/4 \text{ fm}^2$ and 95.8616 fm^2 , respectively. Two different values of r_0 are tested.
 459 One is $r_0 = 1.51 \text{ fm}$ which is the same as the ${}^4\text{He}$ point-nucleon radii in Table IV. The other
 460 is $r_0 = 1.89 \text{ fm}$ corresponding to a swelled core for ${}^6\text{He}$ indicated by r_p in Table IV, assuming
 461 the tetrahedron structure of the “ α core” remains unchanged.

462 A total of three cases are generated for this “nearly symmetric” analytic model. For
 463 convenience, in the following descriptions for the relative distances of the analytic model, the
 464 unbracketed and bracketed values correspond to the results for $r_0 = 1.51 \text{ fm}$ and $r_0 = 1.89 \text{ fm}$
 465 respectively, when they are shown side by side.

466 • Case I: A and B are protons, C and D are neutrons, so the line connecting the
 467 additional two neutrons is parallel to the line connecting the “ α core” two neutrons.

468 i. For np pairs not belonging to the “ α core”, $4|EA|^2 = 4r_{np}^{\prime 2}$;

469

ii. For nn pairs not belonging to the “ α core”, $2|EC|^2 + 2|ED|^2 + |EF|^2 = b$.

By combining and solving i. and ii., one arrives at

$$\begin{aligned} x &= \sqrt{2}r_0 \pm \frac{2\sqrt{3}}{3} \sqrt{r_0^2 - \frac{b}{8} + r_{np}'^2}, \\ w^2 &= \frac{b}{4} - r_{np}'^2 - 2\sqrt{2}xr_0. \end{aligned} \quad (49)$$

470

471

472

473

After substituting the values of r_0 , $r_{np}'^2$ and b into the equations, we get two sets of solutions. The $w^2 > 0$ requirement automatically eliminates the set of solutions in which “+” is chosen for the second term of x . We then obtain $x = -1.264$ fm ($x = -0.971$ fm) and $w = 3.316$ fm ($w = 3.284$ fm).

474

475

476

477

478

479

480

The nucleon position results are illustrated in Fig. 6(a). For $r_0 = 1.51$ fm results, each valence neutron is 3.66 fm from the center of the “ α core”, which is more than double the value of r_0 . While for $r_0 = 1.89$ fm results, each valence neutron is closer to the center of the “ α core” (3.49 fm). On the other hand, the valence neutrons for both r_0 values come very close to the “ α core” neutrons with a minimum separation of 2.19 fm (1.74 fm), which is less than the average separation of nucleons in the “ α core”, 2.47 fm (3.09 fm). Therefore, this configuration does not suggest a halo structure.

481

482

483

484

- Case II: C and D are protons, A and B are neutrons, so the line connecting the additional two neutrons is perpendicular to the line connecting the two “ α core” neutrons.

i. For np pairs not belonging to the “ α core”, $2|EC|^2 + 2|ED|^2 = 4r_{np}'^2$;

ii. For nn pairs not belonging to the “ α core”, $4|EA|^2 + |EF|^2 = b$.

It follows that

$$\begin{aligned} x &= -\sqrt{2}r_0 \pm \frac{2\sqrt{3}}{3} \sqrt{r_0^2 - \frac{b}{8} + r_{np}'^2}, \\ w^2 &= \frac{b}{4} - r_{np}'^2 + 2\sqrt{2}xr_0, \end{aligned} \quad (50)$$

485

486

487

where the set of solutions for the “-” branch of the second term of x will be eliminated by the $w^2 > 0$ requirement. We obtain $x = 1.264$ fm ($x = 0.971$ fm) and $w = 3.316$ fm ($w = 3.284$ fm).

488

489

The resulting positions of nucleons are illustrated in Fig. 6(b). Each valence neutron is again 3.66 fm (3.49 fm) from the center of the “ α core”. Each valence neutron is

490 3.60 fm (3.63 fm) from each of the “ α core” neutrons, 5.15 fm (5.34 fm) from one
 491 proton, and 3.19 fm (2.87 fm) from the other proton. For $r_0 = 1.51$ fm results, all
 492 the two-nucleon separations for nucleon pairs interconnecting the “ α core” and the
 493 valence neutrons are larger than the separations of nucleons in the “ α core”, so this
 494 is a tentative candidate for halo structure of ${}^6\text{He}$. The two valence neutrons form a
 495 118.7° (128.5°) angle with respect to the center of the “ α core”.

496 • Case III: A and C are protons, B and D are neutrons, so the line connecting the
 497 additional two neutrons forms the same angle (60°) with both the line connecting the
 498 “ α core” two protons and the line connecting the “ α core” two neutrons.

- 499 i. For np pairs not belonging to the “ α core”, $2|EA|^2 + |EC|^2 + |ED|^2 = 4r_{np}'^2$;
 500 ii. For nn pairs not belonging to the “ α core”, $2|EA|^2 + |EC|^2 + |ED|^2 + |EF|^2 = b$.

For this configuration, we find

$$x = \pm \frac{\sqrt{6}}{3} \sqrt{2r_{np}'^2 - r_0^2 - \frac{b}{4}}, \quad (51)$$

$$w^2 = \frac{b}{4} - r_{np}'^2,$$

501 Since the resulting w^2 is positive and independent of the value of x , the two solutions
 502 of x are both valid. The first set of solutions is $x = 2.645$ fm ($x = 2.477$ fm) and
 503 $w = 2.365$ fm. The second set of solutions is $x = -2.645$ fm ($x = -2.477$ fm) and
 504 $w = 2.365$ fm.

505 The above two sets of solutions for Case III are illustrated in Fig. 6(c) and (d), re-
 506 spectively. In Fig. 6(c), each valence neutron is 4.01 fm (3.85 fm) from the center of
 507 the “ α core”. The shortest separation between the valence neutrons and the “ α core”
 508 nucleons is 3.57 fm (3.43 fm), larger than in Case II. The valence neutrons form a 68.8°
 509 (71.6°) angle with respect to the center of the “ α core”, which is less than 90° , instead
 510 of an obtuse angle seen in Case II. Therefore, the correlation of the valence nn in this
 511 situation is stronger than in Case II, and it therefore provides a favorable halo picture.
 512 The separation between the valence nn is 4.73 fm (4.73 fm) which is also much shorter
 513 than in Case II, 6.63 fm (6.63 fm).

514 In Fig. 6(d), each valence neutron is again 4.01 fm (3.85 fm) from the center of the “ α
 515 core”. The shortest separation between the valence neutrons and the “ α core” nucleons

516
517
518

is 2.62 fm (2.11 fm), which is similar to (shorter than) the separation between nucleons in the “ α core”, 2.47 fm (3.09 fm). So this is not a candidate for a halo structure of ${}^6\text{He}$.

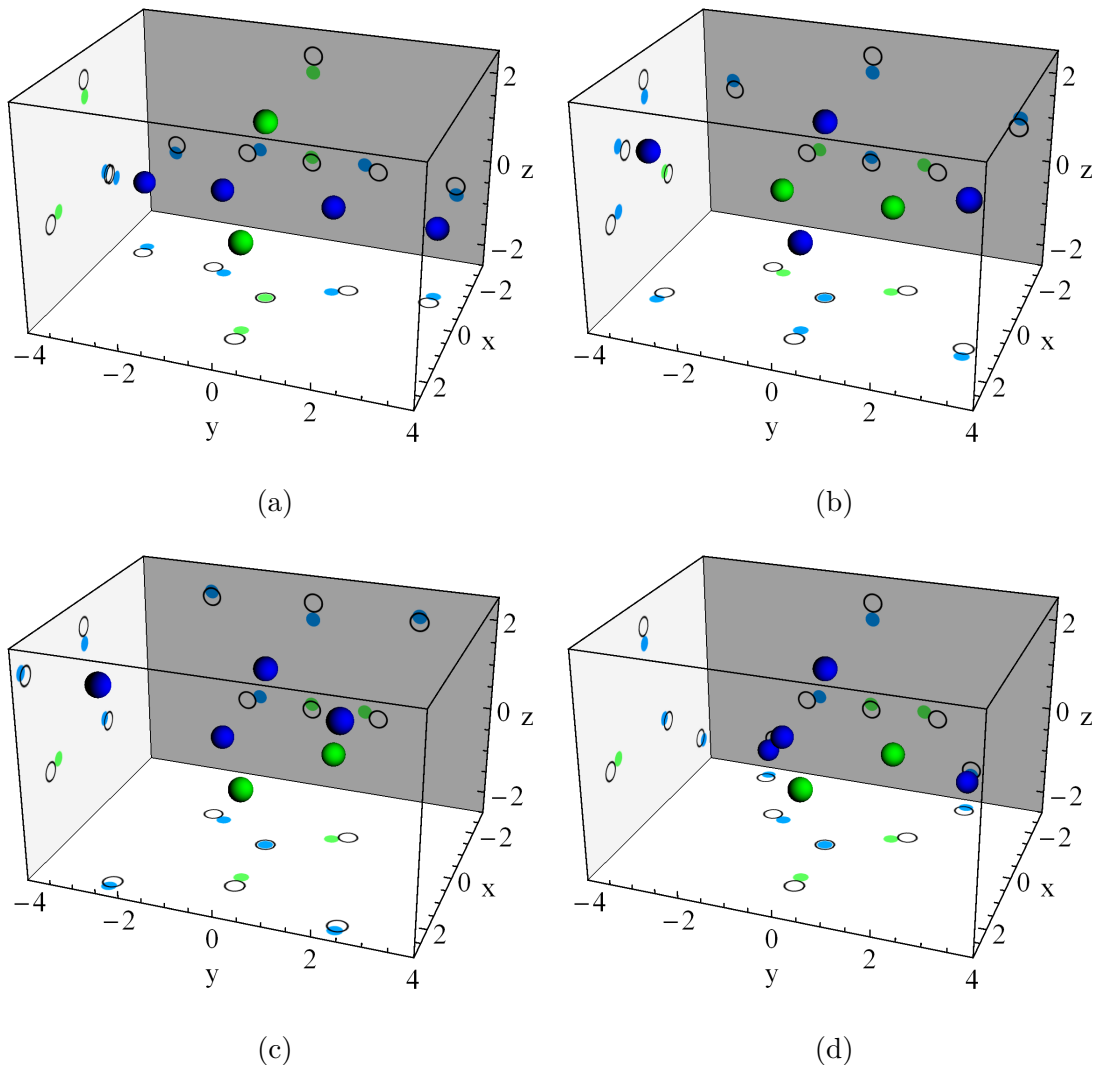


FIG. 6. Results for Case I (a), Case II (b) and Case III (c and d) of the analytic model of ${}^6\text{He}$. The color balls and points show the resulting nucleon positions and their projections on three planes, respectively, for $r_0 = 1.51$ fm, with green (blue) points representing protons (neutrons). The black circles on each projection plane show the projections of nucleon positions for $r_0 = 1.89$ fm.

519
520
521
522

We concluded from the above analysis that it is possible to have a “halo” like structure in the ground state ${}^6\text{He}$ by matching our *ab initio* calculated results to the “nearly symmetric” analytic model, such as the one illustrated in Fig. 6(c). We note that there are several assumptions involved in this analytic model: 1. the searching of the positions for the two

523 valence neutrons is confined on a symmetric plane; 2. the model only fits the total $\langle r^2 \rangle$
524 (summed over the two-body total spins) of pairs with the same isospin projections; 3. we
525 assume a tetrahedron “ α core” throughout the modeling, the shape of which is not allowed
526 to change even in the presence of the two additional neutrons. Despite all the limitations
527 of this model, it is our first attempt towards building 3D models, and it gives us a flavor of
528 a qualitative picture of what the halo structure in ${}^6\text{He}$ could be like. The failure to yield a
529 halo-like structure in Case I suggests that if a halo structure exists, the connecting line of
530 the two valence neutrons is not likely to be parallel to that of the two “ α core” neutrons.
531 The success of obtaining a favorable halo picture in Case III gives us the confidence to pursue
532 a more refined halo picture of ${}^6\text{He}$, which we imagine may share some similar features with
533 the halo picture of Case III (the connecting line of the two valence neutrons forms the same
534 60° angles with both the “ α core” pp connecting line and the “ α core” nn connecting line).
535 This guides us in building a more realistic numerical model, where we are able to partially
536 release the assumed symmetry constraints.

537 B. Numerical model for the dominant two-body total spin configuration

538 From Table I, the ground state ${}^6\text{He}$ two-body total spin configuration provides support
539 for a simple picture based on an “ α core” plus two valence nucleons in a relative spin-
540 singlet state. That is, Table I shows a maximum of 0.14 deviation in pair counts from the
541 simple picture. If we take the number of pairs of a given $\{S, \tau_{za}, \tau_{zb}\}$ to be the same as the
542 corresponding integer (labeled as #pairs) that they are close to in Table I, and multiply
543 by the corresponding $\overline{\langle r^2[S, \tau_{za}, \tau_{zb}] \rangle}$ in Table II, we get $\langle r^2 \rangle$ of the given $\{S, \tau_{za}, \tau_{zb}\}$ for
544 the dominant configuration listed in the first column of Table V. We note that the overall
545 $\langle r^2 \rangle$ of the dominant configuration (205.687 fm^2) is not equal to the sum of $\langle r^2 \rangle$ in Table II
546 (206.718 fm^2). This is not a problem as the dominant configuration is only one of the possible
547 configurations in the ground state ${}^6\text{He}$. The average of $\langle r^2 \rangle$ of all the possible configurations
548 is the more precise result that needs to match the total $\langle r^2 \rangle$ in Table II. We separate the
549 “ α core” part from the remaining part by introducing parameters q , h and g for the square
550 separation of each isospin projected pair, with the two-body total spin configuration of the
551 “ α core” inherited from ${}^4\text{He}$. Then the full set of classical Euclidean distance equations can
552 be solved numerically using any numerical solver such as `scipy.optimize.fsolve` in Python 3.

TABLE V. Numerical model parameter setting of ${}^6\text{He}$ [fm^2] ($\hbar\Omega = 10$ MeV, $N_{\text{max}} = 16$)

S	$\overline{\langle r^2 \rangle} \times \#\text{pairs}$	“ α core” part	remaining part
pp 0	6.85424	6.85424	-
pp 1	0.00000	-	-
np 0	24.7842	q	$24.7842 - q$
np 1	72.9639	$3h$	$72.9639 - 3h$
nn 0	40.5362	g	$40.5362 - g$
nn 1	60.5481	-	60.5481
sum	205.687	-	-

The rms separation between nucleon i and nucleon j is

$$(x_i - x_j)^2 + (y_i - y_j)^2 + (z_i - z_j)^2 = \langle r^2 \rangle_{ij}, \quad (52)$$

553 where $\langle r^2 \rangle_{ij}$ is $\overline{\langle r^2 \rangle} \times \#\text{pairs}$ divided by the number of pairs of given S , $\{\tau_{za}, \tau_{zb}\}$ and part
554 (“ α core” part or the remaining part, as indicated in Table V). The number of equations
555 equals to the number of pairs, $A(A - 1)/2$. Solving a full set of these equations will give us
556 the 3D locations of each nucleon.

557 From the numerical calculation, we get $q = 11.2415$ fm^2 , $h = 2.16994$ fm^2 and $g =$
558 7.08296 fm^2 . The resulting relative locations of ${}^6\text{He}$ nucleons for the dominant two-body spin
559 configuration are illustrated in Fig. 7(b). To our surprise, instead of a perfect tetrahedron,
560 the ${}^6\text{He}$ “ α core” is almost squeezed to a plane, in the presence of the other two neutrons.
561 This phenomenon cannot be observed in the previous analytic model where we assume a
562 tetrahedron “ α core”. To check the validity of this method, we perform a similar numerical
563 calculation for ${}^4\text{He}$, the result of which is shown in Fig. 7(a). As expected, without the
564 presence of the two additional neutrons, ${}^4\text{He}$ itself does form a tetrahedron structure even
565 though we have removed the symmetrical constraint on its shape.

566 For ${}^6\text{He}$, the numerical model gives us the opening angle between the valence neutrons
567 with respect to the center of mass of the “ α core” $\theta_{nn} = 58.1^\circ \lesssim 60^\circ$, indicating the
568 correlation between the valence neutrons and their correlation to the “ α core” are almost
569 the same. This can also be revealed from the separation between the valence neutrons
570 4.09 fm, which is close to the separations between the valence neutrons and the center of
571 mass of the “ α core”, 4.02 fm and 4.38 fm. The near-equilateral configuration of α - n - n can
572 be seen in Fig. 7(d).

573 Regardless of the nearly planar shape of the “ α core”, the solution is, in some sense, a

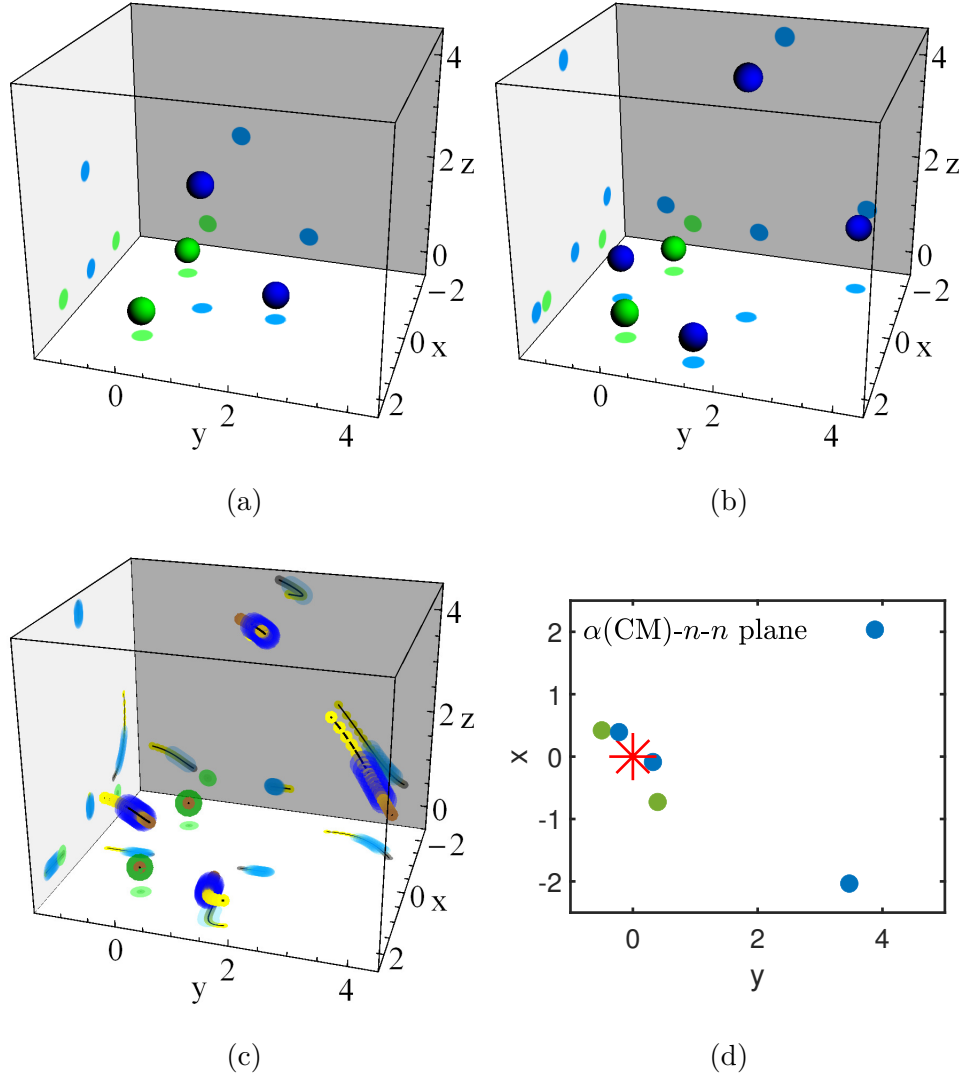


FIG. 7. Results of the numerical model of ${}^4\text{He}$ (a), ${}^6\text{He}$ (b), the modified numerical model of ${}^6\text{He}$ (c) and the numerical model of ${}^6\text{He}$ projecting on the $\alpha(\text{CM})\text{-}n\text{-}n$ plane (d). The green (blue) balls represent protons (neutrons). Three projection planes are shown, with green (blue) dots representing proton (neutron) positions on each projection plane. In (c), the yellowish to brownish points trace the resulting position of nucleons with ξ from -5 fm^2 to 5 fm^2 with increment of 0.5 fm^2 , with more brown color blended in yellow for increasing ξ . The points that belong to the same nucleons are connected in sequence by black lines. The middle of each sequence is overlaid by bigger green (blue) transparent points, which signifies the resulting positions of protons (neutrons) with $-2.3 \text{ fm}^2 \leq \xi \leq 2.7 \text{ fm}^2$. (d) shows the results of the unmodified 3D numerical model (b) projecting on the plane defined by the center of mass (CM) of the “ α core” (labeled by the red asterisk) and the two valence neutrons.

574 mixture of analytic model Case II and Case III. In Case II, “ α core” nn forms a 90° angle
 575 with the valence nn . In Case III, “ α core” pp and nn form the same 60° angles with the
 576 valence nn . In this numerical model, the angle between “ α core” pp and the valence nn is
 577 66.3° and the angle between “ α core” nn and the valence nn is 80.9° .

578 C. Numerical model modification

In Sec. VB, nucleon pairs with the same S and $\{\tau_{za}, \tau_{zb}\}$ provide equally weighted contributions to $\overline{\langle r^2 \rangle} \times \#\text{pairs}$. For example, $3h$ in the “ α core” is shared by three $S = 1$ np pairs with $\langle r^2 \rangle_{ij} = h$ for each pair. $(72.9639 \text{ fm}^2 - 3h)$ in the remaining part is shared by three $S = 1$ np pairs with $\langle r^2 \rangle_{ij} = (72.9639 \text{ fm}^2 - 3h)/3$ for each pair. This is reasonable because almost all the pairs belonging to the same entry in Table V are formed by the same “type” of nucleons (“ α core” protons, “ α core” neutrons, and the two valence neutrons are regarded as three different “types” in this discussion). However, there is one exception which is the $(40.5362 \text{ fm}^2 - g)$ in the entry shared by two $S = 0$ nn pairs in the remaining part. One pair is formed by an “ α core” neutron and a valence neutron ($\langle r^2 \rangle_{ij} = \langle r^2 \rangle'_{nn,S=0}$), and the other pair is formed by the two valence neutrons ($\langle r^2 \rangle_{ij} = \langle r^2 \rangle''_{nn,S=0}$). Thus, the environments surrounding these two pairs inside ${}^6\text{He}$ should be very different if the halo picture is realistic. To account for this difference, we introduce a parameter ξ .

$$\xi \equiv \frac{1}{2} (\langle r^2 \rangle''_{nn,S=0} - \langle r^2 \rangle'_{nn,S=0}). \quad (53)$$

579 Then we solve the numerical model for a sequence of values of ξ with increment of 0.5 fm^2
 580 around $\xi = 0$. The resulting rms separation $r_{ij} = \sqrt{\langle r^2 \rangle_{ij}}$ of each nucleon pair is shown in
 581 Fig. 8. In Fig. 8, “ α core” pairs are denoted by unprimed symbols, pairs interconnecting
 582 “ α core” and the valence neutrons are denoted by primed symbols, and the one pair formed
 583 by the two valence neutrons is denoted by a double-primed symbol. The solid vertical line
 584 at $\xi = 0$ intercepts with results corresponding to the unmodified 3D numerical model in
 585 Sec. VB.

587 Since we don’t know the value of ξ *a priori*, we consider a reasonable range based on
 588 three empirical criteria:

- 589 1. The range of ξ should include $\xi = 0$, which defines the unmodified 3D numerical model
 590 described in Sec. VB.

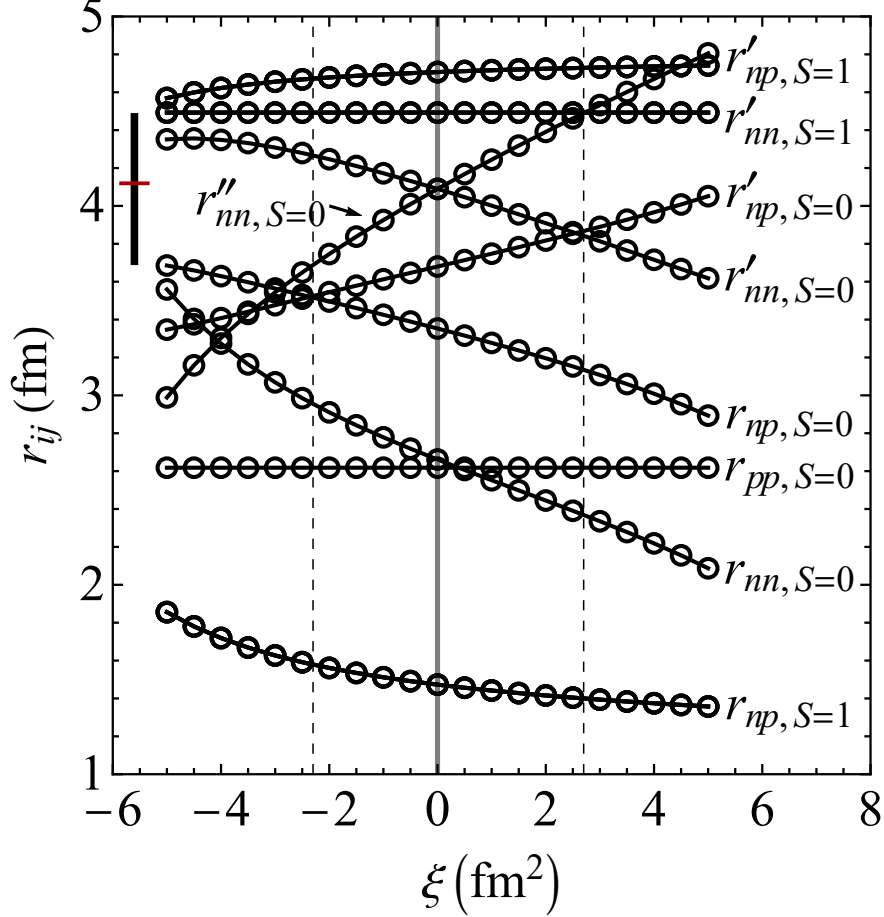


FIG. 8. The rms separation $r_{ij} = \sqrt{\langle r^2 \rangle_{ij}}$ of each pair of nucleons in ${}^6\text{He}$ for the modified numerical model. “ α core” pairs are denoted by unprimed symbols, pairs interconnecting “ α core” and the valence neutrons are denoted by primed symbols, and the one pair formed by the two valence neutrons is denoted by a double-primed symbol. The solid gray vertical line at $\xi = 0$ intercepts with the unmodified 3D numerical model results. The two dashed black vertical lines delineate the bounds of the reasonable range of ξ , $-2.3 \text{ fm}^2 \leq \xi \leq 2.7 \text{ fm}^2$ as discussed in the text. The red horizontal bar on the left of the graph indicates the average value of $r''_{nn,S=0}$ in the reasonable ξ range. The vertical line at the middle of the red horizontal bar is the uncertainty bar of $r''_{nn,S=0}$, which extends over the values obtained in the reasonable range of ξ . The estimated $r''_{nn,S=0} = 4.12^{+0.37}_{-0.43} \text{ fm}$.

591
592
593

2. The rms separation of nucleon pairs in the “ α core” should be smaller than or equal to those interconnecting the “ α core” nucleons with the valence neutrons, otherwise the nucleon we previously labeled as one of the valence neutrons should be re-classified as

594 a nucleon of the nucleon cluster (the “core”), and the one that has longer separations
 595 from other “core” nucleons should be removed from the “core”. If our model still
 596 respects quantum concepts from the shell model of nuclei, the cluster should contain
 597 a closed shell of nuclei, and we just need to switch around the indices of the affected
 598 nucleons or $\langle r^2 \rangle_{ij}$ accordingly. The overall results would not change, only differing by
 599 a sequence of relabelling. As a result, we can obtain the results over a range that does
 600 not require such a relabelling process.

601 3. The relative size of rms separation between $S = 0$ and $S = 1$ pairs should remain
 602 stable throughout the range. Particularly, for pairs with identical isospin projections
 603 (nn and pp), the rms separation for $S = 0$, in general, should be smaller than $S = 1$.
 604 This applies to both ${}^4\text{He}$ and ${}^6\text{He}$, as can be seen in Table II and the analysis followed
 605 by that. Even though we allow a non-zero ξ deviation, we want to keep the results
 606 consistent qualitatively with the previous $\xi = 0$ results.

607 When $\xi < -2.3 \text{ fm}^2$, r'_{np} is less than r_{np} , the second criterion is not satisfied. Thus we
 608 determined the lower bound of the reasonable range of ξ to be around -2.3 fm^2 . For the
 609 third criterion, when comparing $r'_{nn,S=1}$ with $r_{nn,S=0}$, $r'_{nn,S=0}$ and $r''_{nn,S=0}$, we found that in
 610 the range of $\xi \geq -2.3 \text{ fm}^2$, $r_{nn,S=0}$ and $r'_{nn,S=0}$ are always smaller than $r'_{nn,S=1}$. Only $r''_{nn,S=0}$
 611 exceeds $r'_{nn,S=1}$ at around $\xi = 2.7 \text{ fm}^2$ and continues to be larger at even larger values of
 612 ξ , setting the upper bound at $\xi = 2.7 \text{ fm}^2$. Combining the two bounds, we estimated the
 613 reasonable range of ξ to be $-2.3 \text{ fm}^2 \leq \xi \leq 2.7 \text{ fm}^2$.

614 The resulting positions of nucleons are illustrated in Fig. 7(c). Again, the four “ α core”
 615 nucleons are nearly in the same plane, even with a large deviation of ξ from zero. Since
 616 the variable ξ will not change the length of the proton pair, the two protons remain at the
 617 original locations of the unmodified model. We also note that as the pair distance of the
 618 valence neutrons increases, the pair distance of the “ α core” neutrons decreases.

619 Fig. 9 shows the rms point-proton or point-neutron radius of each ${}^6\text{He}$ nucleon for the
 620 modified 3D numerical model as a function of ξ . They are obtained by taking the Euclidean
 621 distances between the resulting nucleon positions and the center of mass of ${}^6\text{He}$. We see a
 622 large gap between the radius of the “ α core” nucleons and that of the two valence neutrons.
 623 In a classical picture, the “ α core” nucleons tend to cluster in the same orbit, while the two
 624 valence neutrons are in higher orbits.

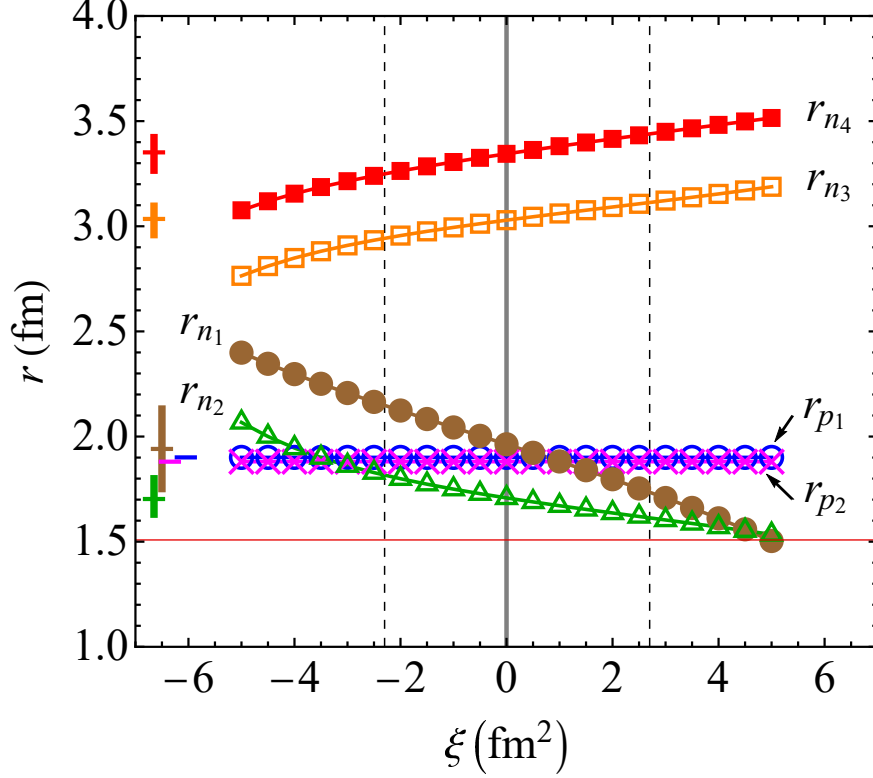


FIG. 9. The point-nucleon rms radius of each ${}^6\text{He}$ nucleon for the modified 3D numerical model. The point-proton (point-neutron) rms radii are labeled as r_{p1} and r_{p2} for the two protons (r_{n1} , r_{n2} , r_{n3} and r_{n4} for the four neutrons), each a different marker/color, to manifest their differences with the traditionally defined point-proton (point-neutron) radius r_p (r_n), which do not distinguish each nucleon. The gray vertical line at $\xi = 0$ intercepts with the results of the unmodified 3D numerical model. The vertical dashed lines delineate the bounds of the reasonable range of ξ , $-2.3 \text{ fm}^2 \leq \xi \leq 2.7 \text{ fm}^2$ as discussed in the text. The point-nucleon rms radius of each nucleon is calculated by averaging the values in the reasonable ξ range and indicated on the left side with a horizontal bar. A vertical uncertainty bar at the middle of the horizontal bar shows the range of these values. The range of the four ${}^4\text{He}$ point-nucleon rms radii calculated by the 3D numerical model is shown by the horizontal red band, which turns out to be narrow indicating a nearly tetrahedron structure for ${}^4\text{He}$.

625 Table VI shows the rms point-nucleon radii for ${}^6\text{He}$ calculated by the 3D numerical
626 model and the modified 3D numerical model compared with the traditional method using
627 Eq. (29) and Eq. (33) with the *ab initio* NCSM calculated results. There is a $\sim 0.5\%$
628 deviation between the 3D numerical model results and the traditional method results, since

629 the 3D numerical model only describes the dominant two-body total spin configuration. The
630 modified 3D numerical model introduces an additional degree of freedom ξ to the numerical
631 model, producing the rms point-nucleon radii with uncertainty ranges that overlap with the
632 traditional method’s results. The average rms point-nucleon radii over a group of nucleons
633 is calculated by taking the root-mean-square of rms point-nucleon radii of the nucleons in
634 the group.

TABLE VI. Results of the point-nucleon rms radii of ${}^6\text{He}$ [fm] ($\hbar\Omega = 10$ MeV, $N_{\text{max}} = 16$). See text for details. The 3D numerical model (“3DNM”) and the modified 3D numerical model (“M3DNM”) are based on the dominant configuration using the *ab initio* NCSM calculated results. The shaded regions represent values for the “ α core”. The average values of 3DNM and M3DNM for each nucleon species are compared with the point-nucleon rms radius traditionally defined (“TD”) and calculated using the *ab initio* NCSM (as in Table IV). The shaded (unshaded) bracketed values are the average values for the “ α core” (the valence neutrons). For an additional comparison, we also show the values obtained by TD for $N_{\text{max}} = 18$ ($\hbar\Omega$ not fixed, corresponding to the minimum Δr in Fig. 1 and Fig. 2.) with a rough and conservative estimation of error by a linear extrapolation of Δr with increasing N_{max} . The experiment values are shown in the last column, where r_n is calculated by r_p and r_m using Eq. (35).

	3DNM	avg.	M3DNM	avg.	TD	TD (18*)	Expt.
r_p	1.90 1.88	1.89	1.90 ^{+0.00} _{-0.00} 1.88 ^{+0.00} _{-0.00}	1.89(0)	1.89	1.90(5)	1.912(18)[57] 1.938(23)/1.953(22)[58]
r_n	1.96 1.71 3.03 3.34	(1.86) 2.60 (3.19)	1.94 ^{+0.21} _{-0.21} 1.70 ^{+0.11} _{-0.09} 3.03 ^{+0.08} _{-0.09} 3.35 ^{+0.09} _{-0.10}	(1.86(8)) 2.60(11) (3.19(9))	2.61	2.64(22)	2.35–3.09
r_m	-	2.39	-	2.39(8)	2.40	2.42(24)	2.23–2.75[56]

635 The point-proton rms radii for the two protons calculated by the 3D numerical model
636 (3DNM) are 1.90 fm and 1.88 fm. For the modified 3D numerical model (M3DNM), because
637 the center of mass of the ${}^6\text{He}$ nucleon system changes due to changing positions of the four
638 neutrons with different ξ , the point-proton rms radii for the two protons are associated with
639 uncertainty ranges which are well below the number of quoted significant figures in Table VI.

640 The average point-proton rms radius over the two protons is about 1.89 fm for both
641 3DNM and M3DNM, which is the same to three significant digits as the point-proton rms

642 radius traditionally defined (TD) and calculated by *ab initio* NCSM shown in Table VI. The
 643 average point-neutron rms radius over the four neutrons for the 3DNM is 2.60 fm which is
 644 close to the 2.61 fm calculated by the TD approach. We note that the M3DNM average
 645 point-neutron rms radius 2.60 ± 0.11 fm overlaps with the TD result. The average point-
 646 nucleon mass rms radius $2.39 (2.39 \pm 0.08)$ fm calculated by the 3DNM (M3DNM) is only
 647 0.01 fm less than the 2.40 fm obtained by the TD approach. The point-nucleon rms radii
 648 for the ground state dominant configuration generated by the 3DNM and by the M3DNM
 649 largely reproduce the *ab initio* NCSM results for the ground state at given N_{\max} and $\hbar\Omega$.
 650 The “ α core” radius 1.86 (1.86 ± 0.08) fm calculated by 3DNM (M3DNM) supports a swelled
 651 “ α core” inside ${}^6\text{He}$ compared with ${}^4\text{He}$ (1.508 ± 0.003 fm calculated by the 3DNM), which
 652 can also be seen in Fig. 9. The valence neutrons have significantly larger average radius 3.19
 653 (3.19 ± 0.09) fm calculated by the 3DNM (M3DNM) compared with the “ α core” radius.

654 We note that $r_{n_1}(r_{n_3})$ is different from $r_{n_2}(r_{n_4})$ and r_{p_1} also has a minor difference with
 655 r_{p_2} . This is due to the fact that the right hand side of Eq. (52) is fixed by the rms separation,
 656 not the rms radius. For example, the four np pairs inside the “core” have one singlet and
 657 three triplets. That one singlet has a different $\langle r^2 \rangle_{ij}$ from those three triplets. So one
 658 neutron inside the “core” forms one np singlet and one np triplet with the protons, and the
 659 other neutron inside the “core” forms two np triplets with the protons (see Fig. 3), resulting
 660 in one closer to the center of mass and the other farther away from the center of mass (of
 661 course the location of the center of mass is determined by all the six nucleons, which is more
 662 complicated).

663 Additionally, we calculate the opening angle of the two valence neutrons with respect to
 664 the center of mass (CM) of the “ α core” θ_{nn} , which is useful for quantifying the correlation
 665 of the two valence neutrons [59]. The results are shown in Fig. 10. We obtain $\theta_{nn} =$
 666 $58.5^{+5.4}_{-6.2}$ degrees, estimated from results in the reasonable range of ξ . We note that the
 667 rms separation of the valence neutrons $4.12^{+0.37}_{-0.43}$ fm illustrated in Fig. 8 overlaps with the
 668 rms separation between the valence neutrons and the CM of the “ α core”, $4.02^{+0.17}_{-0.03}$ fm and
 669 $4.38^{+0.04}_{-0.05}$ fm, computed by the relative distances of the valence neutrons to the CM of the
 670 “ α core” for the M3DNM. So the “ α core” and the two valence neutrons form a nearly
 671 equilateral triangle, reminiscent of the Borromean character of ${}^6\text{He}$.

672 The four-body continuum-discretized coupled-channels (CDCC) method has been applied
 673 to analyzing the scattering data of ${}^6\text{He}$ [60, 61]. ${}^6\text{He}$ was treated as a three-body system

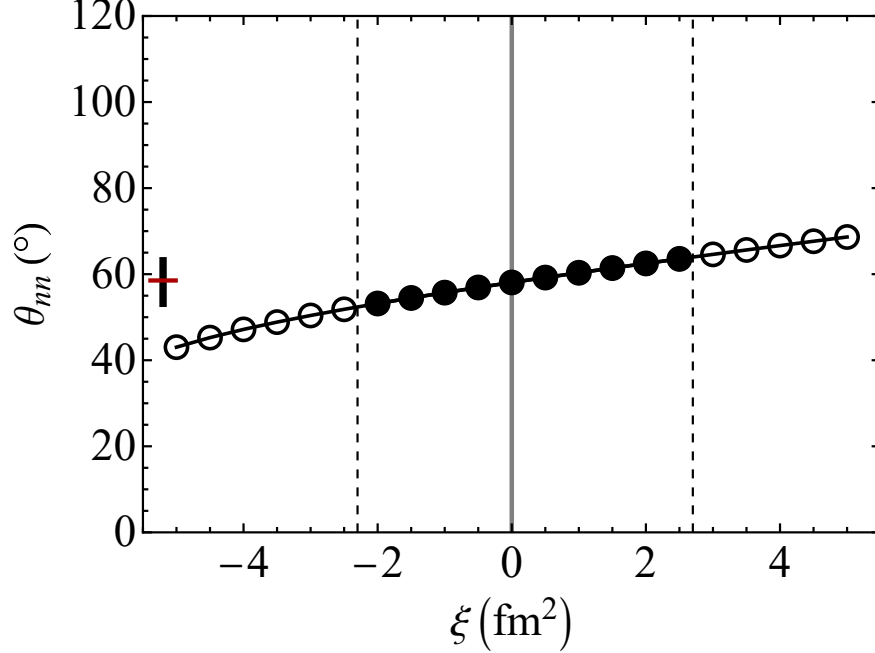


FIG. 10. The opening angle θ_{nn} for ${}^6\text{He}$. The gray vertical line at $\xi = 0$ intercepts with the results corresponding to the unmodified 3D numerical model. The dashed lines delineate the bounds of the reasonable range of ξ , $-2.3 \text{ fm}^2 \leq \xi \leq 2.7 \text{ fm}^2$ as discussed in the text. The red horizontal bar on the left of the graph indicates the average value of θ_{nn} in the reasonable range. The vertical bar at the middle of the red horizontal bar shows the uncertainty of θ_{nn} , which extends over the range of values in the reasonable range of ξ . The estimated $\theta_{nn} = 58.5^{+5.4}_{-6.2}$ degrees.

674 consisting of an inert α -core and two valence neutrons. The scattering wave function of
675 ${}^6\text{He}$ has one bound state and multiple discretized continuum states. A phenomenological αn
676 potential [62] and the Minnesota potential [63, 64] for nn were involved along with the optical
677 potentials for the targets. The $B(E1)$ distribution was extracted from the breakup cross
678 section calculated by the method. The calculated breakup cross section was alternatively
679 adjusted using the experimental data to build an empirical modified CDCC model, assuming
680 all the events are elastic. Geometrical information can then be extracted from both methods,
681 with known matter radii of α and ${}^6\text{He}$ deduced from previous experiments.

682 We compare our θ_{nn} and $\sqrt{r_{nn}^2} = r''_{nn,S=0}$ results from the modified 3D numerical model
683 with the reported values from the CDCC in Table VII. Our result of θ_{nn} is consistent with
684 θ_{nn} of the modified CDCC but $5^\circ \sim 15^\circ$ smaller than that of the unmodified CDCC. θ_{nn} in
685 our work and CDCC are all significantly smaller than the average opening angle of 90° for

686 two noncorrelated neutrons [59], suggesting a sizable dineutron correlation in ${}^6\text{He}$.

TABLE VII. Comparison of geometrical information of ${}^6\text{He}$ from different methods

	Interferometry [65]	CDCC/modified CDCC [60]	This work (M3DNM)
θ_{nn} ($^\circ$)	N.A.	$68/56_{-10}^{+9}$	$58.5_{-6.2}^{+5.4}$
$\sqrt{r_{nn}^2}$ (fm)	5.9 ± 1.2	N.A./4.1(7)	$4.12_{-0.43}^{+0.37}$

687 Our $\sqrt{r_{nn}^2}$ result is also consistent with the one obtained from the modified CDCC. We
688 further compare our $\sqrt{r_{nn}^2}$ result with the one obtained from an interferometry experiment
689 [65]. The upper margin of the range of our $\sqrt{r_{nn}^2}$ result is 0.2 fm smaller than the lower
690 margin of $\sqrt{r_{nn}^2}$ obtained by the interferometry experiment. $\sqrt{r_{nn}^2}$ in our work and the
691 modified CDCC are both smaller than the value obtained by the two-neutron interferometry
692 technique, which is thought to be more sensitive to the higher states instead of the ground
693 state [66].

694 The result of θ_{nn} in our method favors the empirical modified CDCC model over the
695 unmodified CDCC. According to the quoted paper [60], this suggests that the significantly
696 larger breakup cross sections in high E_{rel} region of experimental data compared to the
697 unmodified CDCC results in that region in Fig. 1 of Ref. [60] should be mostly owing to the
698 excess of elastic breakup events at high E_{rel} , rather than inelastic excitations assumed in the
699 unmodified CDCC. Whether this is a common feature for halo nuclei breakup experiments
700 on a heavy target is an interesting and open question.

701 VI. CONCLUSION AND DISCUSSION

702 Our main highlight is that we use a 3D numerical modeling method for the dominant
703 static (“snapshot”) configuration of the ground state ${}^6\text{He}$ based on two-body observables r^0
704 and r^2 calculated by the *ab initio* NCSM. We also build an analytic model that involves
705 symmetry assumptions as an initial trial towards 3D modeling and provides some hints of
706 characteristics for the ${}^6\text{He}$ halo structure.

707 Both the unmodified and modified 3D numerical models of ${}^6\text{He}$ show a large gap between
708 the rms radii of the nucleons within the “ α core” and those outside the “ α core”, which is
709 a clear signature of halo structure. The point-nucleon rms radii from these two models are
710 consistent with those traditionally defined and calculated from *ab initio* NCSM, supporting

711 their use for our static and classical 3D numerical models based only on the dominant
712 configuration of the ground state to infer the geometric properties of the ground state.

713 We obtain a nearly planar shape for the α cluster in ${}^6\text{He}$. This unusual shape is contrary
714 to our intuition that the shape of the α cluster should be similar to the static shape of ${}^4\text{He}$,
715 i.e. a tetrahedron. The altered shape of the α -nucleon system from ${}^4\text{He}$ to ${}^6\text{He}$ is due to
716 the interactions between the two valence neutrons and the α cluster nucleons. That is, in
717 the resulting static configuration of ${}^6\text{He}$, the correlated halo neutrons significantly distort
718 the α -nucleon system from its free-space shape. That is, we obtain a classical version of a
719 significant “core-polarization” effect.

720 In addition, we found a nearly equilateral triangle configuration for the center of mass
721 of the α cluster with the two valence neutrons. The opening angle of the two valence
722 neutrons with respect to the center of mass of the α cluster $\theta_{nn} = 58.5_{-6.2}^{+5.4}$ degrees and
723 the rms separation between the two valence neutrons $\sqrt{r_{nn}^2} = 4.12_{-0.43}^{+0.37}$ fm, both of which
724 are consistent with the results from a phenomenologically modified CDCC method [60].
725 However, our θ_{nn} result is $5^\circ \sim 15^\circ$ smaller than the one from the unmodified CDCC. By
726 comparing with $\sqrt{r_{nn}^2}$ deduced from an interferometry experiment [65], we found that the
727 upper limit of our $\sqrt{r_{nn}^2}$ value is 0.2 fm smaller than the lower limit of the value obtained by
728 this experiment. This may be due to the higher sensitivity of the interferometry experiment
729 to the excited states compared with the ground state.

730 It is intriguing that these elementary, classical and static mathematical models produce
731 consistent results with the literature, using calculated two-body observables from our *ab*
732 *initio* methods as the model input. For larger nuclei, one can ask whether it is possible
733 to develop a systematic mathematical tool for the N -body 3D modeling problem. In this
734 connection, it is interesting to contemplate how far we can go if we also include results of
735 other operators such as r^4 , r^6 and three-body operators. In addition, some of the sym-
736 metry assumptions can be removed, enabling us to turn on a finer and finer resolution for
737 this inferred classical structure of a nucleus, depending on our purpose and the amount
738 of computational resources. Methods for arranging the overall moments in a sequence for
739 reconstructing 3D images can be found in other areas [67, 68], most of which involve sym-
740 metry assumptions and dozens of moments to resolve a satisfactory image. In our *ab initio*
741 method applied here, the intrinsic resolution is limited to the two-body level. Incorporating
742 the multi-body moments will expand upon the two-body information that can be used in

743 the 3D numerical modeling. Finding a mathematical structure for representing the moments
 744 of the two-nucleon density up to some limiting multipolarity appears to be more practical
 745 in the near term.

746 In the future, we aim to apply our method to other nuclear systems associated with
 747 clustering phenomena, such as other halo nuclei ^8He [69], ^{11}Be [70], ^{11}Li [6] and candidates
 748 of multi- α -condensed states [71] ^8Be , $^{12}\text{C}^*(0_2^+)$, ^{16}O etc.. We also aim to test the robustness
 749 of our 3D numerical modeling method using results from *ab initio* NCSM calculation with
 750 different inter-nucleon potentials.

751 VII. ACKNOWLEDGEMENTS

752 This work was supported in part by the US Department of Energy (DOE) under Grant
 753 Nos. DE-FG02-87ER40371 and DE-SC0018223 (SciDAC-4/NUCLEI). Computational re-
 754 sources were provided by the National Energy Research Scientific Computing Center
 755 (NERSC), which is supported by the US DOE Office of Science under Contract No. DE-
 756 AC02-05CH11231. Tobias Frederico thanks the hospitality of the Department of Physics and
 757 Astronomy of the Iowa State University and to the Fulbright Brazil for the financial support
 758 during his visits on 2018 and 2019. TF also thanks CNPq grant 308486/2015-3, INCT-FNA
 759 project 464898/2014-5 and FAPESP Thematic grants 2017/05660-0 and 2019/07767-1.

760 APPENDIX: MOSHINSKY TRANSFORMATION

761 Following closely the notation of Ref. [72], the single particle HO wave functions are

$$\langle \vec{r} | nlm \rangle. \quad (54)$$

762 The two-body oscillator wave function with total AM λ and its projection μ is

$$\langle \vec{r}_1 \vec{r}_2 | n_1 l_1 n_2 l_2 \lambda \mu \rangle = R_{n_1 l_1}(r_1) R_{n_2 l_2}(r_2) \sum_{m_1 m_2} C_{m_1 m_2 \mu}^{l_1 l_2 \lambda} Y_{l_1 m_1}(\Omega_1) Y_{l_2 m_2}(\Omega_2). \quad (55)$$

763 Using the two body relative coordinates

$$\vec{r} = \frac{1}{\sqrt{2}}(\vec{r}_1 - \vec{r}_2) \quad \text{and} \quad \vec{R} = \frac{1}{\sqrt{2}}(\vec{r}_1 + \vec{r}_2), \quad (56)$$

764 one arrives at

$$\langle \vec{r} \vec{R} | n_1 l_1 n_2 l_2 \lambda \mu \rangle = \sum_{lL} \psi_i(r, R) \sum_{mM} C_{mM\mu}^{lL\lambda} Y_{lm}(\mathbf{\Omega}_r) Y_{LM}(\mathbf{\Omega}_R), \quad (57)$$

765 where $i \equiv \{n_1 l_1 n_2 l_2 l L \lambda\}$, and

$$\psi_i(r, R) = \sum_{nN} (nl, NL; \lambda | n_1 l_1, n_2 l_2; \lambda)_1 R_{nl}(r) R_{NL}(R), \quad (58)$$

766 with the well-known Moshinsky brackets $(nl, NL; \lambda | n_1 l_1, n_2 l_2; \lambda)_1$ subscripted by the ratio
767 of the mass of the two bodies (see e.g. [73]).

-
- 768 [1] M. V. Zhukov, B. V. Danilin, D. V. Fedorov, J. M. Bang, I. J. Thompson, and J. S. Vaagen,
769 Bound state properties of Borromean halo nuclei: ${}^6\text{He}$ and ${}^{11}\text{Li}$, *Physics Reports* **231**, 151
770 (1993).
- 771 [2] P. G. Hansen, A. S. Jensen, and B. Jonson, Nuclear halos, *Annual review of nuclear and*
772 *particle science* **45**, 591 (1995).
- 773 [3] A. S. Jensen, K. Riisager, D. V. Fedorov, and E. Garrido, Structure and reactions of quantum
774 halos, *Rev. Mod. Phys.* **76**, 215 (2004).
- 775 [4] B. Jonson, Light dripline nuclei, *AIP Conference Proceedings* **495**, 3 (1999),
776 <https://aip.scitation.org/doi/pdf/10.1063/1.1301722>.
- 777 [5] K. Riisager, Halos and related structures, *Physica Scripta* **T152**, 014001 (2013).
- 778 [6] I. Tanihata, H. Hamagaki, O. Hashimoto, Y. Shida, N. Yoshikawa, K. Sugimoto, O. Yamakawa,
779 T. Kobayashi, and N. Takahashi, Measurements of interaction cross sections and nuclear radii
780 in the light p -shell region, *Phys. Rev. Lett.* **55**, 2676 (1985).
- 781 [7] I. Tanihata, Neutron halo nuclei, *Journal of Physics G: Nuclear and Particle Physics* **22**, 157
782 (1996).
- 783 [8] I. Tanihata, Nuclear physics with RIB's: How it all started, *The European Physical Journal*
784 *Plus* **131**, 90 (2016).
- 785 [9] T. Kobayashi, O. Yamakawa, K. Omata, K. Sugimoto, T. Shimoda, N. Takahashi, and I. Tani-
786 hata, Projectile fragmentation of the extremely neutron-rich nucleus ${}^{11}\text{Li}$ at 0.79 GeV/nucleon,
787 *Phys. Rev. Lett.* **60**, 2599 (1988).

- 788 [10] N. A. Orr, N. Anantaraman, S. M. Austin, C. A. Bertulani, K. Hanold, J. H. Kelley, D. J.
789 Morrissey, B. M. Sherrill, G. A. Souliotis, M. Thoennessen, J. S. Winfield, and J. A. Winger,
790 Momentum distributions of ${}^9\text{Li}$ fragments following the breakup of ${}^{11}\text{Li}$, *Phys. Rev. Lett.* **69**,
791 2050 (1992).
- 792 [11] T. Nakamura, A. M. Vinodkumar, T. Sugimoto, N. Aoi, H. Baba, D. Bazin, N. Fukuda,
793 T. Gomi, H. Hasegawa, N. Imai, M. Ishihara, T. Kobayashi, Y. Kondo, T. Kubo, M. Miura,
794 T. Motobayashi, H. Otsu, A. Saito, H. Sakurai, S. Shimoura, K. Watanabe, Y. X. Watanabe,
795 T. Yakushiji, Y. Yanagisawa, and K. Yoneda, Observation of strong low-lying $E1$ strength in
796 the two-neutron halo nucleus ${}^{11}\text{Li}$, *Phys. Rev. Lett.* **96**, 252502 (2006).
- 797 [12] T. Aumann, D. Aleksandrov, L. Axelsson, T. Baumann, M. J. G. Borge, L. V. Chulkov, J. Cub,
798 W. Dostal, B. Eberlein, T. W. Elze, H. Emling, H. Geissel, V. Z. Goldberg, M. Golovkov,
799 A. Grünschloß, M. Hellström, K. Hencken, J. Holeczek, R. Holzmann, B. Jonson, A. A. Ko-
800 rshenninikov, J. V. Kratz, G. Kraus, R. Kulesa, Y. Leifels, A. Leistenschneider, T. Leth,
801 I. Mukha, G. Münzenberg, F. Nickel, T. Nilsson, G. Nyman, B. Petersen, M. Pfützner,
802 A. Richter, K. Riisager, C. Scheidenberger, G. Schrieder, W. Schwab, H. Simon, M. H. Smed-
803 berg, M. Steiner, J. Stroth, A. Surowiec, T. Suzuki, O. Tengblad, and M. V. Zhukov, Contin-
804 uum excitations in ${}^6\text{He}$, *Phys. Rev. C* **59**, 1252 (1999).
- 805 [13] N. Fukuda, T. Nakamura, N. Aoi, N. Imai, M. Ishihara, T. Kobayashi, H. Iwasaki, T. Kubo,
806 A. Mengoni, M. Notani, H. Otsu, H. Sakurai, S. Shimoura, T. Teranishi, Y. X. Watanabe, and
807 K. Yoneda, Coulomb and nuclear breakup of a halo nucleus ${}^{11}\text{Be}$, *Phys. Rev. C* **70**, 054606
808 (2004).
- 809 [14] C. Romero-Redondo, P. Navrátil, S. Quaglioni, and G. Hupin, *Ab initio* NCSM/RGM for
810 three-body cluster systems and application to ${}^4\text{He} + n + n$, *Few-Body Systems* **55**, 927 (2014).
- 811 [15] S. Quaglioni, P. Navrátil, G. Hupin, J. Langhammer, C. Romero-Redondo, and R. Roth,
812 No-core shell model analysis of light nuclei, *Few-Body Systems* **54**, 877 (2013).
- 813 [16] C. Romero-Redondo, S. Quaglioni, P. Navrátil, and G. Hupin, ${}^4\text{He} + n + n$ continuum within
814 an *ab initio* framework, *Phys. Rev. Lett.* **113**, 032503 (2014).
- 815 [17] P. Navrátil, Cluster form factor calculation in the *ab initio* no-core shell model, *Phys. Rev. C*
816 **70**, 054324 (2004).
- 817 [18] S. Quaglioni, C. Romero-Redondo, P. Navrátil, and G. Hupin, Three-cluster dynamics within
818 the *ab initio* no-core shell model with continuum: How many-body correlations and α clus-

- 819 tering shape ${}^6\text{He}$, Phys. Rev. C **97**, 034332 (2018).
- 820 [19] E. Epelbaum, H. Krebs, T. A. Lähde, D. Lee, and U.-G. Meißner, Structure and rotations of
821 the Hoyle state, Phys. Rev. Lett. **109**, 252501 (2012).
- 822 [20] T. Otsuka, T. Abe, T. Yoshida, Y. Tsunoda, N. Shimizu, N. Itagaki, Y. Utsuno, J. Vary,
823 P. Maris, and H. Ueno, α -Clustering in atomic nuclei from first principles with statistical
824 learning and the Hoyle state character, **13**, 2234 (2022).
- 825 [21] C. Robin, M. J. Savage, and N. Pillet, Entanglement rearrangement in self-consistent nuclear
826 structure calculations, Phys. Rev. C **103**, 034325 (2021).
- 827 [22] B. R. Barrett, P. Navrátil, and J. P. Vary, *Ab initio* no core shell model, Progress in Particle
828 and Nuclear Physics **69**, 131 (2013).
- 829 [23] C. Cockrell, J. P. Vary, and P. Maris, Lithium isotopes within the *ab initio* no-core full
830 configuration approach, Phys. Rev. C **86**, 034325 (2012).
- 831 [24] C. Cockrell, *Ab initio nuclear structure calculations for light nuclei (2012)*, Ph.D. thesis, Iowa
832 State University (2012).
- 833 [25] H. Georgi, *Lie Algebras in Particle Physics: From Isospin to Unified Theories (2nd ed.)* (CRC
834 Press, 1999).
- 835 [26] A. R. Edmonds, *Angular Momentum in Quantum Mechanics* (Princeton University Press,
836 2016).
- 837 [27] S. Bacca, N. Barnea, and A. Schwenk, Matter and charge radius of ${}^6\text{He}$ in the hyperspherical-
838 harmonics approach, Phys. Rev. C **86**, 034321 (2012).
- 839 [28] M. A. Caprio, P. Maris, and J. P. Vary, Coulomb-Sturmian basis for the nuclear many-body
840 problem, Phys. Rev. C **86**, 034312 (2012).
- 841 [29] M. A. Caprio, P. Maris, and J. P. Vary, Halo nuclei ${}^6\text{He}$ and ${}^8\text{He}$ with the Coulomb-Sturmian
842 basis, Phys. Rev. C **90**, 034305 (2014).
- 843 [30] P. A. Zyla et al. (Particle Data Group), Prog. Theor. Exp. Phys. 2020, 083C01 (2020)., .
- 844 [31] R. A. M. Basili, *Nuclear properties with effective operators (2019)*, Ph.D. thesis, Iowa State
845 University (2019).
- 846 [32] J. Carlson, V. Pandharipande, and R. Wiringa, Three-nucleon interaction in 3-, 4- and ∞ -body
847 systems, Nuclear Physics A **401**, 59 (1983).
- 848 [33] S. C. Pieper, V. R. Pandharipande, R. B. Wiringa, and J. Carlson, Realistic models of pion-
849 exchange three-nucleon interactions, Phys. Rev. C **64**, 014001 (2001).

- 850 [34] S. Coon, M. Scadron, P. McNamee, B. Barrett, D. Blatt, and B. McKellar, The two-pion-
851 exchange three-nucleon potential and nuclear matter, *Nuclear Physics A* **317**, 242 (1979).
- 852 [35] P. Maris, M. Sosenkina, J. P. Vary, E. Ng, and C. Yang, Scaling of ab-initio nuclear physics
853 calculations on multicore computer architectures, *Procedia Computer Science (ICCS 2010)* **1**,
854 97 (2010).
- 855 [36] H. M. Aktulga, C. Yang, E. G. Ng, P. Maris, and J. P. Vary, Improving the scalability of a sym-
856 metric iterative eigensolver for multi-core platforms, *Concurrency and Computation: Practice
857 and Experience* **26**, 2631 (2014), <https://onlinelibrary.wiley.com/doi/pdf/10.1002/cpe.3129>.
- 858 [37] P. Maris, E. Epelbaum, R. J. Furnstahl, J. Golak, K. Hebeler, T. H  ther, H. Kamada,
859 H. Krebs, U.-G. Meißner, J. A. Melendez, A. Nogga, P. Reinert, R. Roth, R. Skibiński,
860 V. Soloviov, K. Topolnicki, J. P. Vary, Y. Volkotrub, H. Witała, and T. Wolfgruber (LENPIC
861 Collaboration), Light nuclei with semilocal momentum-space regularized chiral interactions
862 up to third order, *Phys. Rev. C* **103**, 054001 (2021).
- 863 [38] P. Maris, R. Roth, E. Epelbaum, R. J. Furnstahl, J. Golak, K. Hebeler, T. H  ther, H. Kamada,
864 H. Krebs, H. Le, U.-G. Meißner, J. A. Melendez, A. Nogga, P. Reinert, R. Skibiński, J. P. Vary,
865 H. Witała, and T. Wolfgruber, Nuclear properties with semilocal momentum-space regularized
866 chiral interactions beyond N2LO, arXiv:2206.13303 [nucl-th] (2022).
- 867 [39] A. Shirokov, I. Shin, Y. Kim, M. Sosenkina, P. Maris, and J. Vary, N3LO *NN* interaction
868 adjusted to light nuclei in *ab exitu* approach, *Physics Letters B* **761**, 87 (2016).
- 869 [40] F. Wegner, Flow-equations for Hamiltonians, *Annalen der Physik* **506**, 77 (1994),
870 <https://onlinelibrary.wiley.com/doi/pdf/10.1002/andp.19945060203>.
- 871 [41] S. D. Glazek and K. G. Wilson, Perturbative renormalization group for Hamiltonians, *Phys.*
872 *Rev. D* **49**, 4214 (1994).
- 873 [42] W. N. Polyzou and W. Gl  ckle, Three-body interactions and on-shell equivalent two-body
874 interactions, *Few-Body Systems* **9**, 97 (1990).
- 875 [43] I. J. Shin, *Ab initio* calculations for Li isotopes with Daejeon16, in *Proceedings of the Ito*
876 *International Research Center Symposium "Perspectives of the Physics of Nuclear Structure"*,
877 <https://journals.jps.jp/doi/pdf/10.7566/JPSCP.23.013008>.
- 878 [44] Y. Kim, I. J. Shin, A. M. Shirokov, M. Sosenkina, P. Maris, and J. P. Vary, Daejeon16 *NN*
879 interaction, arXiv:1910.04367 [nucl-th] (2019).
- 880 [45] P. Maris, I. J. Shin, and J. P. Vary, *Ab initio* structure of *p*-shell nuclei with chiral effective

- 881 field theory and Daejeon16 interactions, arXiv:1908.00155 [nucl-th] (2019).
- 882 [46] P. Papakonstantinou, J. P. Vary, and Y. Kim, Daejeon16 interaction with contact-term cor-
883 rections for heavy nuclear systems, *J. Phys. G* **48**, 085105 (2021).
- 884 [47] A. M. Shirokov, A. I. Mazur, I. A. Mazur, E. A. Mazur, I. J. Shin, Y. Kim, L. D. Blokhintsev,
885 and J. P. Vary, Nucleon- α scattering and resonances in ^5He and ^5Li with JISP16 and Daejeon16
886 NN interactions, *Phys. Rev. C* **98**, 044624 (2018).
- 887 [48] A. I. Mazur, A. M. Shirokov, I. A. Mazur, L. D. Blokhintsev, Y. Kim, I. J. Shin, and J. P.
888 Vary, Description of continuum states within the no-core shell model: Single-state HORSE
889 method, *Physics of Atomic Nuclei* **82**, 537 (2019).
- 890 [49] I. A. Mazur, A. M. Shirokov, A. I. Mazur, I. J. Shin, Y. Kim, P. Maris, and J. P. Vary,
891 Description of continuum spectrum states of light nuclei in the shell model, *Physics of Particles
892 and Nuclei* **50**, 537 (2019).
- 893 [50] A. M. Shirokov, Y. Kim, A. I. Mazur, I. A. Mazur, I. J. Shin, and J. P. Vary,
894 Tetraneutron resonance: Theory, *AIP Conference Proceedings* **2038**, 020038 (2018),
895 <https://aip.scitation.org/doi/pdf/10.1063/1.5078857>.
- 896 [51] I. A. Mazur, I. J. Shin, Y. Kim, A. I. Mazur, A. M. Shirokov, P. Maris, and J. P.
897 Vary, SS-HORSE extension of the no-core shell model: Application to resonances in ^7He ,
898 arXiv:2207.07360 [nucl-th] (2022).
- 899 [52] G. A. Negoita, J. P. Vary, G. R. Luecke, P. Maris, A. M. Shirokov, I. J. Shin, Y. Kim, E. G.
900 Ng, C. Yang, M. Lockner, and G. M. Prabhu, Deep learning: Extrapolation tool for *ab initio*
901 nuclear theory, *Phys. Rev. C* **99**, 054308 (2019).
- 902 [53] P. Cappellaro, Chapter 5. Nuclear Structure, in *22.02 Introduction to Applied Nuclear Physics.
903 Spring 2012* (MIT OpenCourseWare. License: Creative Commons BY-NC-SA. Massachusetts
904 Institute of Technology, Cambridge, MA, 2012).
- 905 [54] K. Hagino and H. Sagawa, Pairing correlations in nuclei on the neutron-drip line, *Phys. Rev.
906 C* **72**, 044321 (2005).
- 907 [55] G. Papadimitriou, A. T. Kruppa, N. Michel, W. Nazarewicz, M. Płoszajczak, and J. Rotureau,
908 Charge radii and neutron correlations in helium halo nuclei, *Phys. Rev. C* **84**, 051304 (2011).
- 909 [56] Z.-T. Lu, P. Mueller, G. W. F. Drake, W. Nörtershäuser, S. C. Pieper, and Z.-C. Yan, Collo-
910 quium: Laser probing of neutron-rich nuclei in light atoms, *Rev. Mod. Phys.* **85**, 1383 (2013).
- 911 [57] L.-B. Wang, P. Mueller, K. Bailey, G. W. F. Drake, J. P. Greene, D. Henderson, R. J. Holt,

- 912 R. V. F. Janssens, C. L. Jiang, Z.-T. Lu, T. P. O'Connor, R. C. Pardo, K. E. Rehm, J. P.
 913 Schiffer, and X. D. Tang, Laser spectroscopic determination of the ${}^6\text{He}$ nuclear charge radius,
 914 Phys. Rev. Lett. **93**, 142501 (2004).
- 915 [58] M. Brodeur, T. Brunner, C. Champagne, S. Ettenauer, M. J. Smith, A. Lapierre, R. Ringle,
 916 V. L. Ryjkov, S. Bacca, P. Delheij, G. W. F. Drake, D. Lunney, A. Schwenk, and J. Dilling,
 917 First direct mass measurement of the two-neutron halo nucleus ${}^6\text{He}$ and improved mass for
 918 the four-neutron halo ${}^8\text{He}$, Phys. Rev. Lett. **108**, 052504 (2012).
- 919 [59] Y. Kubota, A. Corsi, G. Authelet, H. Baba, C. Caesar, D. Calvet, A. Delbart, M. Dozono,
 920 J. Feng, F. Flavigny, J.-M. Gheller, J. Gibelin, A. Giganon, A. Gillibert, K. Hasegawa,
 921 T. Isobe, Y. Kanaya, S. Kawakami, D. Kim, Y. Kikuchi, Y. Kiyokawa, M. Kobayashi,
 922 N. Kobayashi, T. Kobayashi, Y. Kondo, Z. Korkulu, S. Koyama, V. Lapoux, Y. Maeda, F. M.
 923 Marqués, T. Motobayashi, T. Miyazaki, T. Nakamura, N. Nakatsuka, Y. Nishio, A. Obertelli,
 924 K. Ogata, A. Ohkura, N. A. Orr, S. Ota, H. Otsu, T. Ozaki, V. Panin, S. Paschalis, E. C. Pol-
 925 lacco, S. Reichert, J.-Y. Roussé, A. T. Saito, S. Sakaguchi, M. Sako, C. Santamaria, M. Sasano,
 926 H. Sato, M. Shikata, Y. Shimizu, Y. Shindo, L. Stuhl, T. Sumikama, Y. L. Sun, M. Tabata,
 927 Y. Togano, J. Tsubota, Z. H. Yang, J. Yasuda, K. Yoneda, J. Zenihiro, and T. Uesaka, Surface
 928 localization of the dineutron in ${}^{11}\text{Li}$, Phys. Rev. Lett. **125**, 252501 (2020).
- 929 [60] Y. Sun, T. Nakamura, Y. Kondo, Y. Satou, J. Lee, T. Matsumoto, K. Ogata, Y. Kikuchi,
 930 N. Aoi, Y. Ichikawa, K. Ieki, M. Ishihara, T. Kobayshi, T. Motobayashi, H. Otsu, H. Saku-
 931 rai, T. Shimamura, S. Shimoura, T. Shinohara, T. Sugimoto, S. Takeuchi, Y. Togano, and
 932 K. Yoneda, Three-body breakup of ${}^6\text{He}$ and its halo structure, Physics Letters B **814**, 136072
 933 (2021).
- 934 [61] M. Rodríguez-Gallardo, J. M. Arias, J. Gómez-Camacho, A. M. Moro, I. J. Thompson, and
 935 J. A. Tostevin, Four-body continuum-discretized coupled-channels calculations, Phys. Rev. C
 936 **80**, 051601 (2009).
- 937 [62] H. Kanada, T. Kaneko, S. Nagata, and M. Nomoto, Microscopic study of nucleon- ${}^4\text{He}$ scat-
 938 tering and effective nuclear potentials, Progress of Theoretical Physics **61**, 1327 (1979).
- 939 [63] D. Thompson, M. Lemere, and Y. Tang, Systematic investigation of scattering problems with
 940 the resonating-group method, Nuclear Physics A **286**, 53 (1977).
- 941 [64] Y. Tang, M. LeMere, and D. Thompson, Resonating-group method for nuclear many-body
 942 problems, Physics Reports **47**, 167 (1978).

- 943 [65] F. Marqués, M. Labiche, N. Orr, J. Angélique, L. Axelsson, B. Benoit, U. Bergmann, M. Borge,
944 W. Catford, S. Chappell, N. Clarke, G. Costa, N. Curtis, A. D'Arrigo, F. de Oliveira Santos,
945 E. de Góes Brennand, O. Dorvaux, M. Freer, B. Fulton, G. Giardina, C. Gregori, S. Grévy,
946 D. Guillemaud-Mueller, F. Hanappe, B. Heusch, B. Jonson, C. Le Brun, S. Leenhardt, M. Le-
947 witowicz, M. López, K. Markenroth, M. Motta, A. Mueller, T. Nilsson, A. Ninane, G. Nyman,
948 I. Piqueras, K. Riisager, M. Saint Laurent, F. Sarazin, S. Singer, O. Sorlin, and L. Stuttgé,
949 Two-neutron interferometry as a probe of the nuclear halo, *Physics Letters B* **476**, 219 (2000).
- 950 [66] N. A. Orr, Neutron-neutron correlations in the dissociation of halo nuclei, arXiv:0803.0886
951 [nucl-ex] (2008).
- 952 [67] V. John, I. Angelov, A. Öncül, and D. Thévenin, Techniques for the reconstruction of a
953 distribution from a finite number of its moments, *Chemical Engineering Science* **62**, 2890
954 (2007).
- 955 [68] J. Bruner, *Image analysis by moments: reconstruction and computational aspects* (Oficyna
956 Wydawnicza Politechniki Wrocławskiej, Wrocław, Poland, 2006).
- 957 [69] P. Mueller, I. A. Sulai, A. C. C. Villari, J. A. Alcántara-Núñez, R. Alves-Condé, K. Bailey,
958 G. W. F. Drake, M. Dubois, C. Eléon, G. Gaubert, R. J. Holt, R. V. F. Janssens, N. Lècesne,
959 Z.-T. Lu, T. P. O'Connor, M.-G. Saint-Laurent, J.-C. Thomas, and L.-B. Wang, Nuclear
960 charge radius of ^8He , *Phys. Rev. Lett.* **99**, 252501 (2007).
- 961 [70] J. H. Kelley, S. M. Austin, R. A. Kryger, D. J. Morrissey, N. A. Orr, B. M. Sherrill, M. Thoen-
962 nessen, J. S. Winfield, J. A. Winger, and B. M. Young, Parallel momentum distributions as a
963 probe of halo wave functions, *Phys. Rev. Lett.* **74**, 30 (1995).
- 964 [71] T. Kokalova, N. Itagaki, W. von Oertzen, and C. Wheldon, Signatures for multi- α -condensed
965 states, *Phys. Rev. Lett.* **96**, 192502 (2006).
- 966 [72] M. Znojil, Moshinsky brackets for light nuclei, *Phys. Rev. C* **15**, 423 (1977).
- 967 [73] M. Sotona and M. Gmitro, Generalized transformation brackets for the harmonic oscillator
968 functions, *Computer Physics Communications* **3**, 53 (1972).